Initiation of a Supercell by Convectively Generated Gravity Waves in the Simulated Kaiyuan Tornadic Event of 3 July 2019

HAOJIA LI,[a,b] MING XUE,[b] KEFENG ZHU,[c] AND XIN XU[a]

[a] *Key Laboratory of Mesoscale Severe Weather/Ministry of Education and School of Atmospheric Sciences, Nanjing University, Nanjing, China*
[b] *Center for Analysis and Prediction of Storms and School of Meteorology, University of Oklahoma, Norman, Oklahoma*
[c] *CMA Key Laboratory of Transportation Meteorology, Nanjing Joint Institute for Atmospheric Sciences, Nanjing, China*

(Manuscript received 30 October 2023, in final form 28 August 2024, accepted 26 September 2024)

ABSTRACT: An EF4-rated supercell tornado occurred on 3 July 2019 in Kaiyuan, China, causing heavy casualties. A three-level nested-grid high-resolution numerical simulation is used to investigate the initiation of the tornadic supercell. Automatic weather station (AWS) data, *FY-4A* visible satellite data, and Doppler radar data are used to verify the model simulation. The most important aspects of the simulated presupercell mesoscale convective system (MCS) and the initiation of the supercell agree with observations. Detailed investigation of the model results reveals that the initial cells form first above a convective boundary layer (CBL) on the dry side of a surface dryline. Above the CBL is a moist layer in terms of relative humidity, and the layer is stable. Convectively generated gravity waves (GWs) emanating from the MCS and propagating southward along the stable layer above the CBL provide localized forcing for the actual triggering of initial cells at specific locations. The associated perturbation potential temperature and vertical velocity patterns confirm that the GWs trigger a series of cloud bands. The additional lifting by the updraft of a horizontal convective roll in the CBL underneath the GW updraft works together to promote faster growth of the initial cell that later becomes the supercell. Examination of the Scorer parameter profiles shows favorable conditions for vertical trapping of GWs along the waveguide in the stable layer, preventing the radiation of wave energy to the upper levels.

SIGNIFICANCE STATEMENT: This study reveals an atypical initiation mechanism of a tornadic supercell that occurred on 3 July 2019 in northern China. By analyzing high-resolution numerical simulation results and observations, the supercell is found to be initially triggered by convectively generated gravity waves (GWs) propagating along a moist and stable layer above the convective boundary layer. The GWs were excited by vigorous convection along the leading-edge gust front of a mesoscale convective system to the north. The vertical atmospheric structure acts to trap the gravity wave energy to the stable layer and supports the horizontal propagation of the GWs away from their sources. Our study indicates the elevated initiation mechanism of convection by convectively generated GWs, providing a better understanding of this type of convective initiation that is typically difficult to predict.

KEYWORDS: Convective-scale processes; Inertia-gravity waves; Supercells; Numerical analysis/modeling

1. Introduction

Deep moist convection (DMC), such as supercells, is responsible for a large portion of severe weather, including heavy precipitation, hail, and tornadoes, in China (Luo et al. 2020; Meng et al. 2016; Sun et al. 2019; Wei et al. 2022; Zheng et al. 2020) and in other parts of the world. Considering its tremendous impact, the initiation of DMC is of great interest to forecasters. However, the initiation of convection is often poorly predicted in numerical weather prediction (NWP) models, leading to forecast failures (Browning et al. 2007; Wilson and Roberts 2006).

To improve forecasting skills of convective initiation (CI), a better understanding of the initiation mechanisms is of great importance. In recent years, CI has received more attention (Bai et al. 2019; e.g., Markowski et al. 2006; Weckwerth and Parsons 2006; Xue and Martin 2006a,b) and was a subject of research in a number of field campaigns, including Convection Initiation and Downburst Experiment (CINDE) (Wilson et al. 1988), convective available potential energy (CAPE) (Wilson and Megenhardt 1997), International H_2O Project (IHOP_2002) (Weckwerth et al. 2004; Wilson and Roberts 2006), Understanding Severe Thunderstorms and Alberta Boundary Layers Experiment (UNSTABLE) (Taylor et al. 2011), and Plains Elevated Convection at Night (PECAN) (Geerts et al. 2017). Studies have found that airmass boundaries—including drylines, gust fronts, sea-breeze fronts, mountain–valley winds, and synoptic fronts—and their interactions often provide conducive mesoscale lifting forcings for CI (Droegemeier and Wilhelmson 1985; Wang and Xue 2012, 2018; Wang et al. 2016; Weiss and Bluestein 2002; Xue and Martin 2006b; Zhang et al. 2021).

Apart from those surface-based boundaries, convection can also be initiated by orographic forcing (Lean et al. 2009; Rasmussen and Houze 2016), bores (Haghi et al. 2019; Parsons et al. 2019; Wilson and Roberts 2006), and gravity waves (GWs; Schmidt and Cotton 1990; Stobie et al. 1983; Uccellini and Koch 1987; Zhang et al. 2001). Convectively generated GWs can significantly impact the development of new convection and

Corresponding author: Ming Xue, mxue@ou.edu

DOI: 10.1175/MWR-D-23-0248.1

associated storm environments, as evidenced by numerous studies (Bretherton and Smolarkiewicz 1989; Du and Zhang 2019; Lac et al. 2002; Mapes 1993; Su and Zhai 2017; Wilson et al. 2018). For example, the pioneering work by Mapes (1993) found that a heat source with a vertical profile of observed tropical mesoscale convective systems could cause upward displacement at low levels in its surrounding environment.

Convectively generated GWs can be divided into low- and high-frequency waves, depending on their wave frequencies. Low-frequency GWs are mainly generated by deep, transient diabatic heating and cooling within a convective storm (Lane and Reeder 2001) and are often characterized by different modes of diabatic heating profiles (Nicholls et al. 1991), while high-frequency GWs are mainly generated by cyclical redevelopment of convective cells (McAnelly et al. 1997) or nonlinear advection of buoyancy (Lane and Reeder 2001). Due to their distinct characteristics, these two types of waves can have different effects on CI. The low-frequency waves prepare the surrounding environment for CI through general ascent at the lower troposphere associated with different wave modes (Adams-Selin 2020; Fovell 2002; Fovell et al. 2006; Lane and Reeder 2001), while high-frequency GWs can provide localized forcings to trigger new convection (Adams-Selin and Johnson 2013; Fovell et al. 2006). For the former, using a two-dimensional cloud-resolving model, Lane and Reeder (2001) found that the first three GW modes generated by modeled convection significantly modify the cloud environment and make it more favorable for the development of new convection. For the latter, Fovell et al. (2006) used idealized simulations to investigate the mechanisms of discrete cell propagation within a midlatitude squall line and found that the ducted high-frequency gravity waves emanating from the convective region in the main storm helped cumulus clouds form ahead of the original line.

Low-frequency hydrostatic GWs can propagate horizontally without any additional trapping mechanism other than tropopause reflection if the vertical heating profile is a harmonic of the depth of the troposphere. On the other hand, high-frequency nonhydrostatic GWs will lose most of their energy to vertical propagation if no trapping mechanism exists (Alexander and Holton 2004; Fovell et al. 1992; Nicholls et al. 1991). The wave trapping mechanism has been widely used to explain long-lived GW events in both observational and numerical simulation studies (Bosart et al. 1998; Koch et al. 1988; Liu et al. 2018; Powers and Reed 1993; Zhang et al. 2001).

Although the above studies have improved our understanding of GW CI, real-case studies involving GW CI are still relatively few, and the potential impacts of interactions between GWs with other convergent boundaries, such as drylines and gust fronts, on CI are even less understood. The observational study of Marsham et al. (2011) is one of few in this area. During the IHOP_2002 (Weckwerth et al. 2004), one CI episode was found to occur at the intersection of an elevated convergence line (at the terminus of a nocturnal low-level-jet) with a propagating GW based on radar observations. The initiated elevated convection eventually evolved into a ground-based squall line. The Scorer parameter (Crook 1988; Scorer 1949) based on sounding data was found to be consistent with the trapping of GWs.

The present study focuses on the CI of a tornadic supercell that occurred in Kaiyuan City, Liaoning Province, northeastern China, on 3 July 2019. On that day, a series of convective cells developed ahead of the gust front of a major mesoscale convective system (MCS), and one of the cells evolved into a supercell that spawned an EF4 tornado (Zhang et al. 2020). Previous studies on this case suggested that the interaction between a surface dryline and the gust front of a preceding MCS played a key role in the initiation of the tornadic supercell (Yuan et al. 2021; Zheng et al. 2020). However, these studies mainly focused on meso-β-scale features based on relatively coarse observations, while the actual triggering process of DMC at the specific locations was not investigated in any depth. The exact triggering mechanism, including the possible role of the dryline, if any, is still uncertain. To understand the CI process of this case, we resort to a high-resolution numerical simulation with the aid of available observations in this study. A three-level nested-grid numerical simulation, with a 450-m grid spacing on the inner-most grid, is performed. High-frequency outputs of the simulation give us the ability to track the supercell from its beginning and analyze its initiation mechanism. High-frequency GWs triggered by the MCS convection and their propagation ahead of the gust front within an elevated stable moist layer are found to play key roles in the initiation of the modeled supercell.

The rest of this paper is organized as follows. An overview of the case to be studied is introduced in section 2. The setup of the numerical experiment is described in section 3. In section 4, simulation results are verified against radar and automatic weather station (AWS) observations. The evolution of a dryline and the MCS gust front, as well as their possible effects on supercell CI, are then discussed. The development and characteristics of convectively generated GWs, their forcing on CI, and the vertical trapping mechanism for GWs are also discussed in this section. A summary will be provided in section 5.

2. Case overview

A violent tornado, rated EF4 on the enhanced Fujita scale, occurred in Kaiyuan, Liaoning Province, on the afternoon of 3 July 2019, causing seven fatalities and 190 injuries in total (Zhang et al. 2020). It was one of seven EF4-intensity tornadoes that have been recorded in China and the first EF4-rated case in Liaoning Province (see Fig. 4 for locations) in northeast China (Zheng et al. 2020). The parent tornadic storm first appeared at the southwestern end of an MCS at 1638 LST (hereafter all times are LST, which is 8 h ahead of UTC) and grew rapidly into a supercell in the next 30 min while moving southeastward to Kaiyuan (Zheng et al. 2020). At around 1715 LST, the tornado occurred north of Kaiyuan City and moved southward along with the storm. In the end, it dissipated at 1747 LST (Zhang et al. 2020).

The synoptic patterns are illustrated in Fig. 1. At 1400 LST, 3 July 2019, a quasistationary northeast China cold vortex (NCCV) (Fan et al. 2023; Sun et al. 1994; Xie and Bueh 2015)

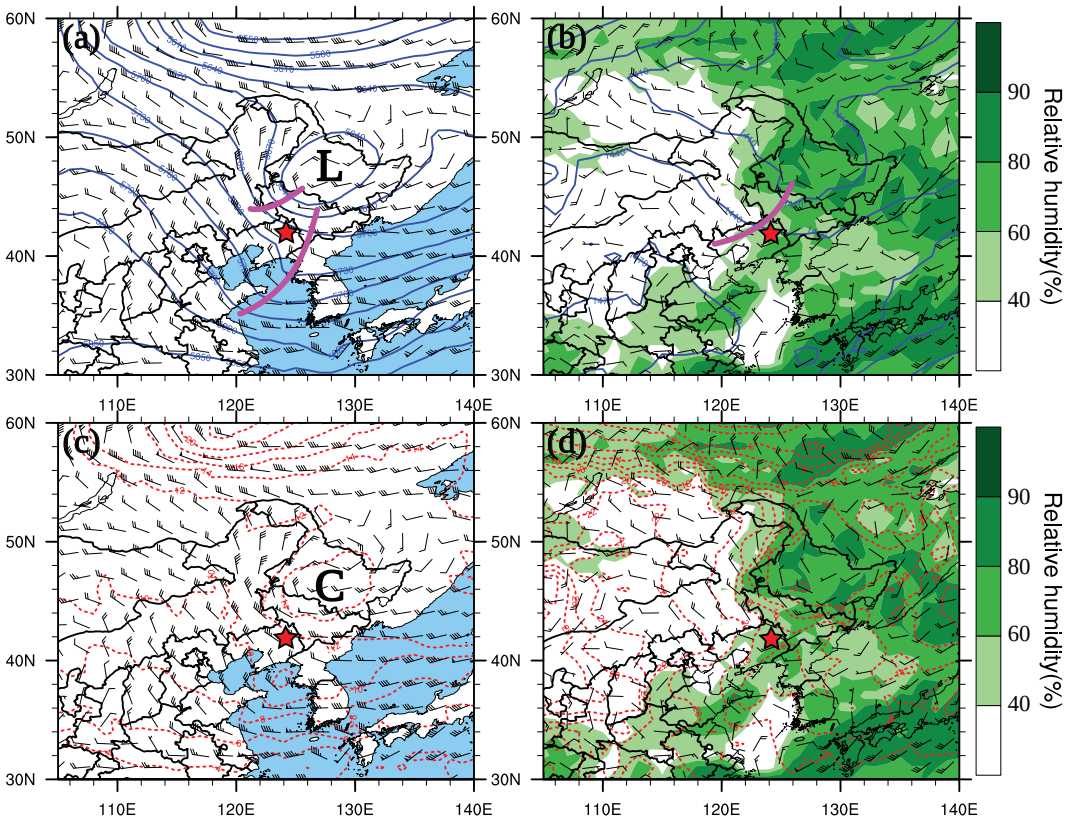

FIG. 1. (a),(b) Geopotential height (thick blue contours; 30-m interval), (c),(d) temperature (dashed red contours; °C), and wind barbs (a full barb represents 5 m s^{-1}, and a half barb represents 2.5 m s^{-1}) plotted from NCEP GFS FNL analysis at 1400 LST 3 Jul 2019, at the 500-hPa level in (a) and (c) and at the 850-hPa level in (b) and (d). The shaded areas in (b) and (d) represent the 850-hPa RH field. Bold pink lines are trough lines, and the red star marks Kaiyuan City. Bold labels L and C denote the low pressure center and cold center, respectively.

as a cutoff low is prominent at 500 hPa over northeast China (Fig. 1a). The cold vortex extends southwestward along a trough line on the 500 hPa, while another deep trough further east extends southward over the Bohai Bay and then southwestward to the south of the Shandong Peninsula. At 850 hPa, a closed circulation is found underneath the 500-hPa cold vortex, with a trough line extending southwestward ahead of the 500-hPa trough and right behind Kaiyuan (red star in Fig. 1). At Kaiyuan, strong northwesterly flow at the bottom of the cold vortex is found at 500 hPa, while at 850 hPa, the flow is southwesterly ahead of the trough. At the lower levels, such southwesterly flow passes over Bohai Bay and is rich in moisture. The strong northwesterly upper-level flow overlaying the moisture-rich southwesterly low-level flow creates strong vertical wind shear and provides favorable conditions for intense deep convection (Fig. 1a).

Meanwhile, a surface low is located near the southeastern corner of Inner Mongolia, reaching into western Jilin and northern Liaoning provinces (Fig. 2; locations of the provinces are shown in Fig. 4). A dryline with strong moisture contrast extends from ahead of the surface low southwestward along the Bohai Bay coastal line of Hebei Province (Fig. 2a). The water vapor mixing ratio q_v on the moist (east) side of the dryline is about 8 g kg^{-1} higher than the dry (west) side. The winds are from the northwest behind the dryline, while those east of the dryline are southwesterly, corresponding to strong directional shift and convergence of winds (Fig. 2a). Such a dryline is often observed in warm seasons in northeastern China between the dry air masses from the Greater Khingan Range and the moist air masses from the Bohai Bay (Fang et al. 2020). East of the dryline, CAPE values range between ~600 and ~1500 J kg^{-1} and approach 2000 J kg^{-1} further northeast in central Jilin Province (Fig. 2b) where we hypothesize that an MCS generated gravity waves that later triggered the tornadic supercell storm.

The development and evolution of the MCS and the supercell can be seen in *Fengyun-4A* (*FY-4A*) geostationary satellite visible images of 0.5-km resolution, taken at 1338, 1430, 1615, and 1730 LST 3 July 2019. At 1338 LST, a quasilinear MCS system with a bow shape at the leading edge (pointed to by the red arrow in Fig. 3a) has already developed over central Jilin Province. There was another MCS to its northeast in Heilongjiang Province (Fig. 3a). This quasilinear MCS grew in length and intensity (Fig. 3b) and will be shown later in radar reflectivity to consist of a line of convective cells that are almost connected (compare Fig. 5c). During this period, a

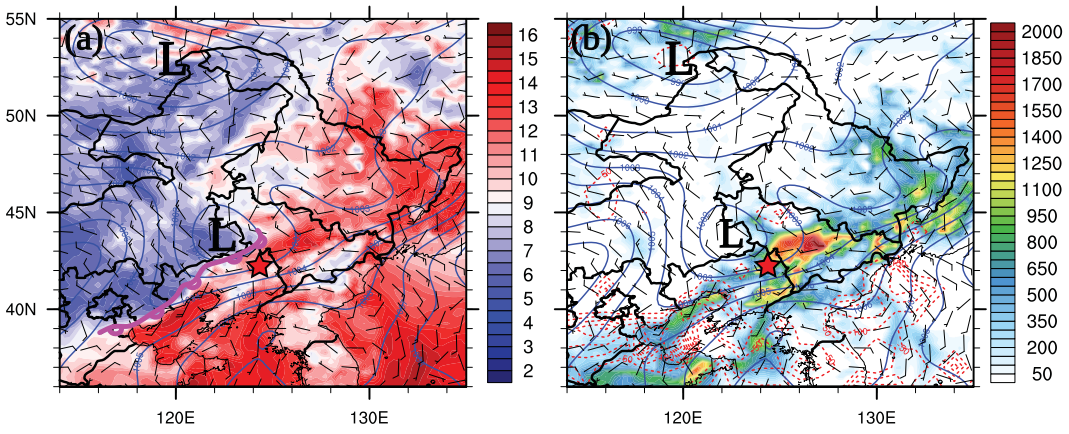

FIG. 2. The surface fields plotted from FNL analysis at 1400 LST 3 Jul 2019: (a) Geopotential height (thick blue contours; 1 m), water vapor mixing ratio q_v (shaded; g kg^{-1}), and the wind fields (full barb represents 5 m s^{-1}, and half barb represents 2.5 m s^{-1}); (b) wind fields, geopotential height (thick blue contours; 1 m), CAPE (shaded; J kg^{-1}), and CIN (dashed red contours; J kg^{-1}). Dryline is marked by standard symbols in pink. Bold letter L denotes the surface low center, and the red star marks Kaiyuan City.

series of cloud bands formed to the southwest of the MCS, in the red boxes in Figs. 3a and 3b. These cloud bands should be located on the dry side of the surface dryline indicated in Fig. 2a, and therefore, they are not the typical clouds/convection developing over the dryline convergence zone (e.g., Xue and Martin 2006a,b), as will be discussed in more details later.

By 1615 LST, the cloud anvils of the MCS have expanded in coverage and moved southeastward. Its southwestern end

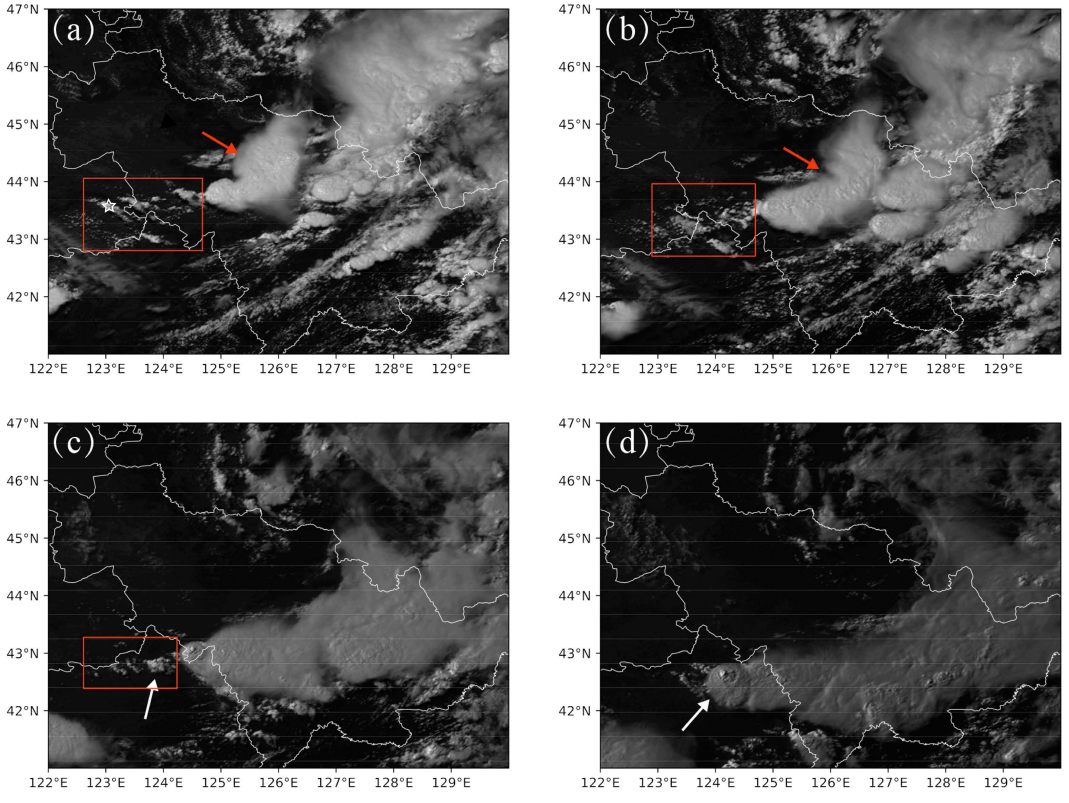

FIG. 3. Visible satellite images from the geostationary *FY-4A* satellite of China, taken at (a) 1338, (b) 1430, (c) 1615, and (d) 1730 LST 3 Jul 2019. The red boxes indicate the locations of convectively generated clouds. The white star in (a) indicates the location of the Tongliao sounding shown in Fig. 11a. The red arrows point to the presupercell MCS. The white arrows indicate the supercell and its initial cell.

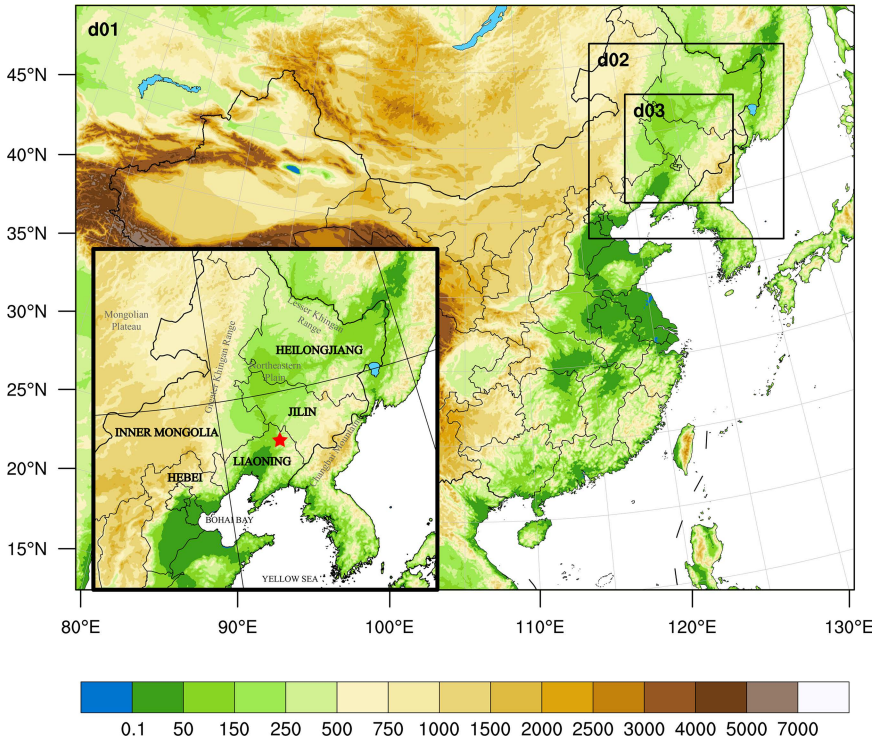

FIG. 4. Model domains D1, D2, and D3 with 4050-, 1350-, and 450-m grid spacings, respectively, together with shaded terrain elevation. The inset is over northeastern China showing the locations of major mountains and seas and the names of provinces. The red star marks the location of Kaiyuan City.

has reached northern Liaoning Province (Fig. 3c). The earlier cloud bands southwest of the MCS grew into a few closely located convective cells (pointed to by the white arrow in Fig. 3c), and by 1730 LST, the convection has developed a pronounced overshooting top surrounded by an anvil that is connected with the anvil of MCS on its northeast side (see the white arrow in Fig. 3d). This overshooting top has often been recognized as a feature that can precede severe convective hazards (Fujita 1989). Clearly, the convection developed very quickly and organized into a single dominant cell over the 75-min period from 1615 to 1730 LST (Figs. 3c,d). In fact, this dominant cell is the supercell that spawned the EF4 tornado in Kaiyuan during this period.

3. Model configuration

The WRF-ARW model version 4.0.3 (Skamarock et al. 2019) is used to perform a real-data simulation of this case. The model is set up with three two-way nested domains, with horizontal grid spacings of 4050, 1350, and 450 m, respectively. These domains are called D1, D2, and D3, respectively (Fig. 4). The outer domain D1 spans the entire continental China, while the inner domains D2 and D3 cover the northeastern China and the entire MCS, respectively. There are 51 vertical levels from the surface to the 50-hPa model top. The vertical grid is stretched with a minimum spacing of 26 m near the ground, and there are 10 model levels within the lowest 1 km.

The model used the two-moment Morrison microphysical scheme (Morrison and Grabowski 2008), the Pleim–Xiu land surface and surface layer models (Pleim 2006), the Asymmetric Convective Model, version 2 (ACM2), PBL scheme (Pleim 2007), and the Community Atmosphere Model, version 3.0 (CAM3.0), radiation scheme for longwave and shortwave radiation (Collins et al. 2004) on all three domains. None of these grids used cumulus parameterizations. The same set of physics was used for real-time forecasts during the summer seasons over a number of years in China, and the forecasts exhibited a high level of skill in forecasting warm-season precipitation (Zhu et al. 2018). In Zhu and Xue (2016), this physical configuration was found to perform the best among a number of physical combinations for an extreme rainfall case in northern China.

All three domains are initialized from the 0000 UTC (0800 LST) 3 July 2019 NCEP Global Forecast System (GFS) final (FNL) analysis and integrated for 12 h. The boundary conditions are provided by the GFS forecasts every 3 h. For D3, the model history files at 2-min intervals are saved to capture the fast evolution around CI. For D1 and D2, 10-min interval outputs are saved.

4. Results

a. Simulation verification

In this section, data from Doppler weather radars and AWSs are first used to verify the simulation (Fig. 5). At 0900 LST,

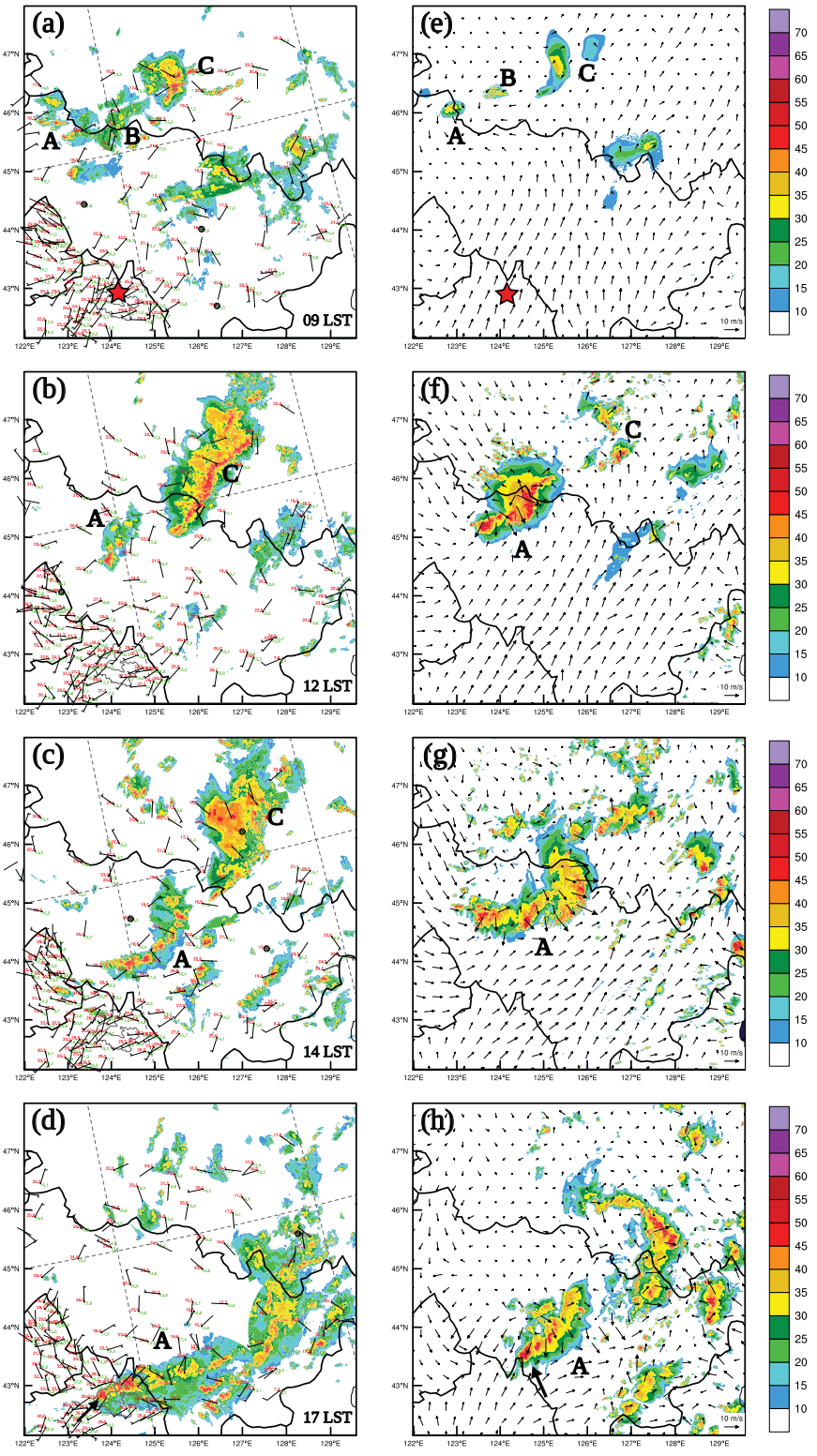

FIG. 5. Temperature (red texts; °C), dewpoint (green texts; °C), wind barbs (full and half barbs represent 10 and 5 m s^{-1}, respectively) at the AWSs and observed radar composite reflectivity (shaded) at (a) 0900, (b) 1200, (c) 1400, and (d) 1700 LST 3 Jul 2019. (e)–(h) D3-simulated composite reflectivity at the corresponding times, together with horizontal wind vectors at the first model level above ground. The red star in (a) and (b) denotes the location of Kaiyuan. Labels A, B, and C denote the observed and simulated convective systems.

scattered convective cells, labeled A, B, and C, were observed on the border of Jilin and Heilongjiang provinces (Fig. 5a) in composite radar reflectivity. Over the next 3 h, cells B and C merged and developed into a much stronger quasilinear convective system (QLCS) labeled C. Meanwhile, cell A developed separately and moved to the southwest of the QLCS (Fig. 5b). By 1400 LST, the original QLCS had entered its weakening stage, whereas cell A expanded and formed a line of cells with a bow shape (labeled line A) and the line became almost connected with the weakening QLCS to its north (Fig. 5c). In the following hours, line A expanded further in length and maintained intensity at its southern end while moving southeastward (Fig. 5d). Line A also became further connected with the weakening convection to its northeast. Such evolution was also seen earlier based on satellite images in Fig. 3.

The overall evolution of convection is reasonably well captured by the model on the 450-m grid although discrepancies in details do exist (right panels of Fig. 5). At 0900 LST, the model reproduces convective cells A, B, and C at about the right locations with similar characteristics as observed (Figs. 5a,e). By 1200 LST, the northern portion of the QLCS weakens and moves east faster than observed, while cell B appears to have moved further south and merged with cell A (Fig. 5f) instead of with cell C as was observed (Fig. 5b). At 1400 LST, the general organization of convection is close to observed, with a bow-shaped line in the south and weakened QLCS with a moderate bow in the north (Figs. 5c,g). Over the next 3 h by 1700 LST, the model-simulated convection in the south moves southeastward as observed, but the location is not as far south and east as observed (Figs. 5d,h). The gust front/outflow boundary associated with the convection can be clearly identified by the curved convergence line between northerly outflows and southerly and southwesterly flows to their south in the simulation and less clearly by the surface station wind observations. Most important to this study is an accurate model representation of the intense supercell storm at the southernmost end of MCS convection. While there are timing and location errors and discrepancies between the convection organizations, the evolution of the physical processes is in a reasonable agreement between model simulation and observation, considering that convective-scale details are difficult to predict accurately. For this study, we are most concerned with the initiation mechanism of the supercell given the preexisting MCS.

In Fig. 6, we examine the fields in zoomed-in domains near the locations and times of supercell CI in the observations and simulation. Because of the location displacement error, the observation and simulation domains shown are not identical. At 1636 LST, three individual cells initially formed at a distance to the southwestern end of the MCS (pointed to by the black arrow in Fig. 6a). A detailed check on the temperature and wind fields surrounding these cells indicates that they were initiated ahead of the gust front associated with the cold pool of the MCS (Fig. 6a), suggesting a mechanism of "action at a distance." After that, the southwestmost cell merged with the other two and developed rapidly into a supercell at around 1700 LST (see the black arrow in Fig. 6b). The model reproduces similar behaviors, with three initial cells forming to the southwest of the leading convective line of MCS and ahead of the associated gust front (Fig. 6d), although the lineup of the three cells is different from observation. The cells in the model also merged and intensified in the subsequent hours and bear some similarity in appearance to the observation (Fig. 6e). By 1654 LST, the merged cell has evolved into a DMC and showed some supercellular characteristics in terms of an updraft core with maximum vertical velocity exceeding 30 m s^{-1} and a midlevel mesocyclone with strong cyclonically rotating winds (Fig. 6f).

There are discrepancies between the simulation and observations, including the northward displacement of the locations of the CI and later supercell and the difference in the timing of CI. We attribute the timing difference in the CI between observation and simulation to the stronger MCS intensity at its southwestern end in simulation (Figs. 5c,g). The more intense convective activity in simulation causes the earlier triggering of convectively generated GWs, and the GWs will be shown to be responsible for the initiation of convection that evolves into the supercell later. The location error is mainly due to the position error of the gust front and cold pool of the MCS that have evolved for several hours in the model simulation. The morphology, including the orientation of the reflectivity anvil, is also quite different in the simulated supercell compared to the observed. In the observation, the reflectivity anvil is mostly east and southeast of the hook echo, while in the simulation, it is mostly to the north of the hook (Figs. 6c,f). We attribute this discrepancy to the mid-to-upper-level storm-relative flows in the simulation that are southerly instead of northerly (not shown). This is apparently due to the fact that the simulated cold pool, being reinforced by the cold pool of the simulated MCS, is too strong, leading to too fast southward propagation of the supercell and, as a result, the northward or rearward upper-level storm-relative flows. Our ongoing experiments assimilating local radar and surface observations produce better evolution of the modeled supercell and correct orientation of the reflectivity anvil, partly through improving the MCS cold pool. Given that the focus of this study is on the initiation of the cells that evolved into supercells, we are less concerned about the inaccuracy in the later evolution of the supercell. We are most concerned with the locations of the CI and where they are relative to the MCS, especially relative to its outflow boundary or gust front, and the physical processes primarily responsible for the initiation of these cells. In subsequent sections, we will focus on these processes by analyzing model simulation data.

b. *The evolution of dryline, CBL, and initiation of clouds above CBL*

Figure 7 shows simulated q_v and wind vectors in domain D3 at the lowest model level above ground. At 1030 LST, a noticeable dryline exists along the border between Inner Mongolia and Liaoning Province (Fig. 7a). At this stage, cells A and B discussed earlier (compare Fig. 5) have just formed and produced weak cold pools on the ground (Fig. 7a). Compared to the observed dryline discussed earlier in section 2, the simulated dryline here is the northern portion of the

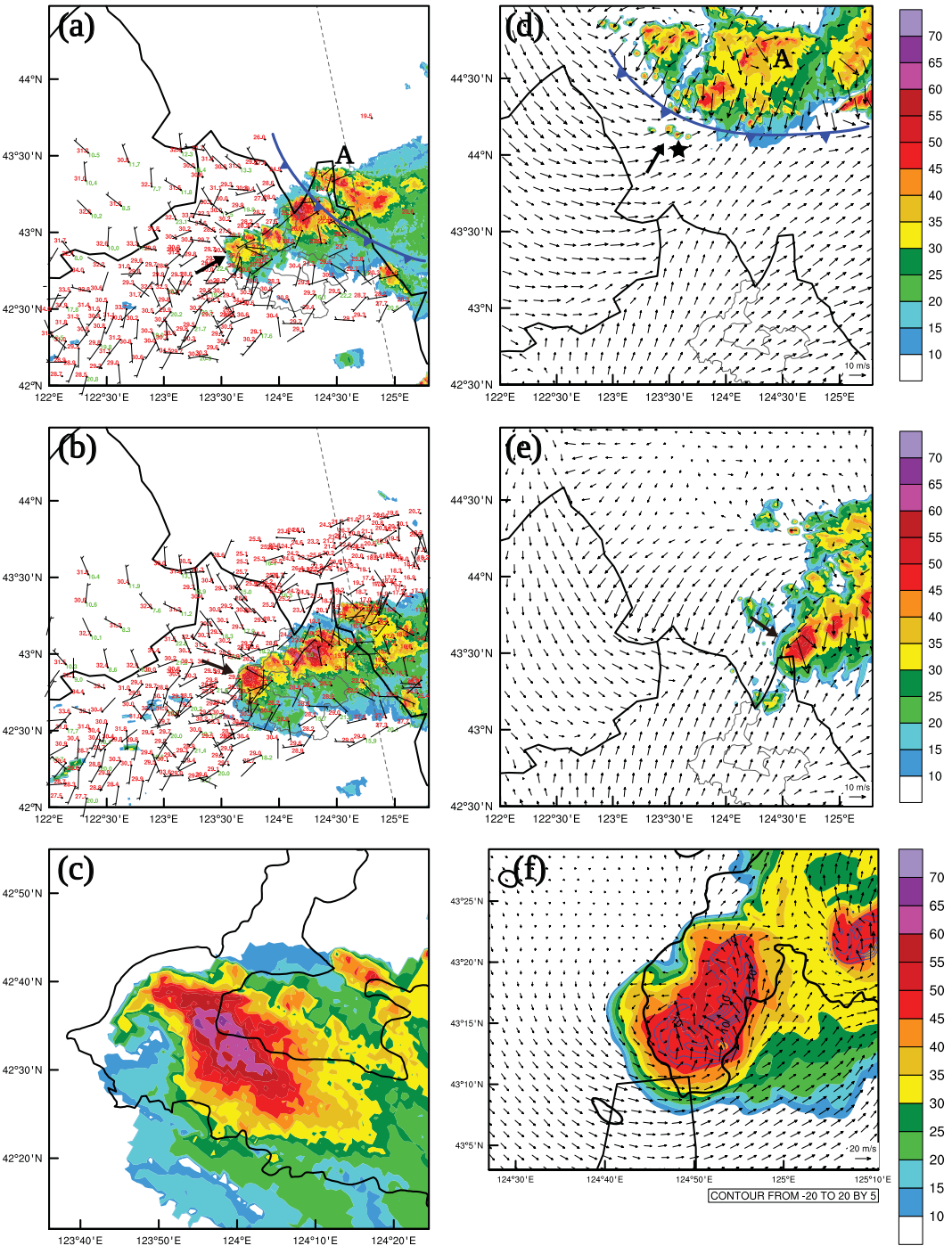

FIG. 6. Temperature (red texts; °C), dewpoint (green texts; °C), wind barbs (full and half barbs for 10 and 5 m s^{-1}) at the AWSs and observed radar composite reflectivity (shaded) at (a) 1636 and (b) 1700 LST 3 Jul 2019. D3-domain-simulated composite reflectivity (shaded) and wind vectors at the lowest model level (~26 m AGL) at (d) 1446 and (e) 1700 LST. (c) Observed radar composite reflectivity of the supercell storm at 1736 LST and (f) D3-simulated reflectivity (shaded), vertical velocity (blue contours at intervals of 5 m s^{-1}), and horizontal wind vectors at the 4 km AGL at 1654 LST. The 20-dBZ reflectivity indicated by the thick black contour in (f) is also plotted to outline the hook echo of the storm. The subjectively analyzed gust fronts are indicated by the blue front symbols. The black arrows indicate the observed and simulated supercells and their initial cells. The black star in (d) denotes the location of the extracted sounding profile shown in Fig. 11b.

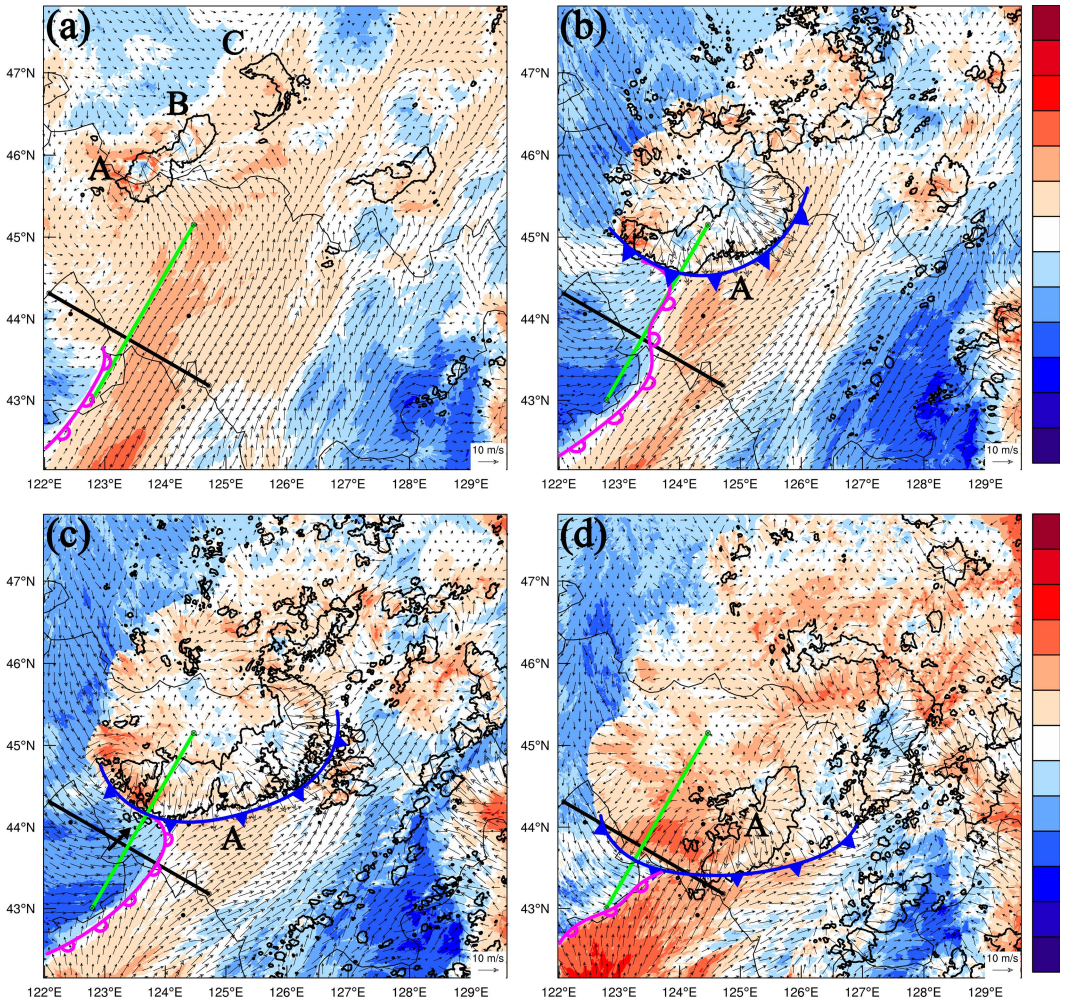

FIG. 7. D3-simulated water vapor mixing ratio q_v (shaded; g kg^{-1}) and horizontal wind vectors at the first model level above ground at (a) 1030, (b) 1330, (c) 1500, and (d) 1700 LST. The simulated composite reflectivity (black contours; dBZ) greater than 20 dBZ is also shown. The green and black lines indicate vertical cross sections shown in Figs. 8 and 9.

observed one (Fig. 2a). In the vertical cross section along the black line in Fig. 7a, relatively moist air occupies most of the mixed CBL of about 1 km deep and the along-line moisture gradient is weak at this location (Fig. 8a). The gradient is much larger south of this cross section (Fig. 7a).

By 1330 LST, the convective cells seen in Fig. 7a have developed into an MCS with a strong cold pool and an arching gust front pushing southward. The dryline has moved eastward and extended northward to intersect the gust front (Fig. 7b). In the subsequent hours, the MCS cold pool continued to expand and the gust front moved further south, eroding the north part of the dryline (Figs. 7c,d). In the vertical cross sections along the black line in Fig. 7, the mixed CBL is seen to deepen with time, with the CBL top on the dry (west) side of the dryline reaching 2.5 km at 1230 LST (Fig. 8b) and about 3 km at 1330 and 1500 LST (Figs. 8c,d). The CBL is shallower on the east side of the dryline, increasing from ~1.2 km at 1230 LST to ~2 km at 1500 LST. The stronger CBL mixing on the dry side brings dryer air from above to the surface, enhancing the moisture gradient at the dryline. It also transports higher westerly momentum to the surface, pushing the dryline eastward while enhancing wind convergence there. Similar processes are commonly observed with drylines occurring in the western Great Plains of the United States (Crawford and Bluestein 1997). The most common CI locations are along the dryline where low-level convergence is enhanced (e.g., Xue and Martin 2006b), but in this case, the initial CIs occur on the west side of the dryline, as will be discussed next.

In the cross sections along the green line in Fig. 7 that is more or less parallel to the dryline, we can see where early cells are initiated (Figs. 8e–h). At 1030 LST, the cross section is still located on the east side of the dryline (Figs. 7a and 8e), and the boundary layer is moist, shallow, and capped by an inversion. At 1330 LST, the cross section is located within the cold pool at its northern end, close to the dryline in the middle section, and west of the dryline at its southern one-third

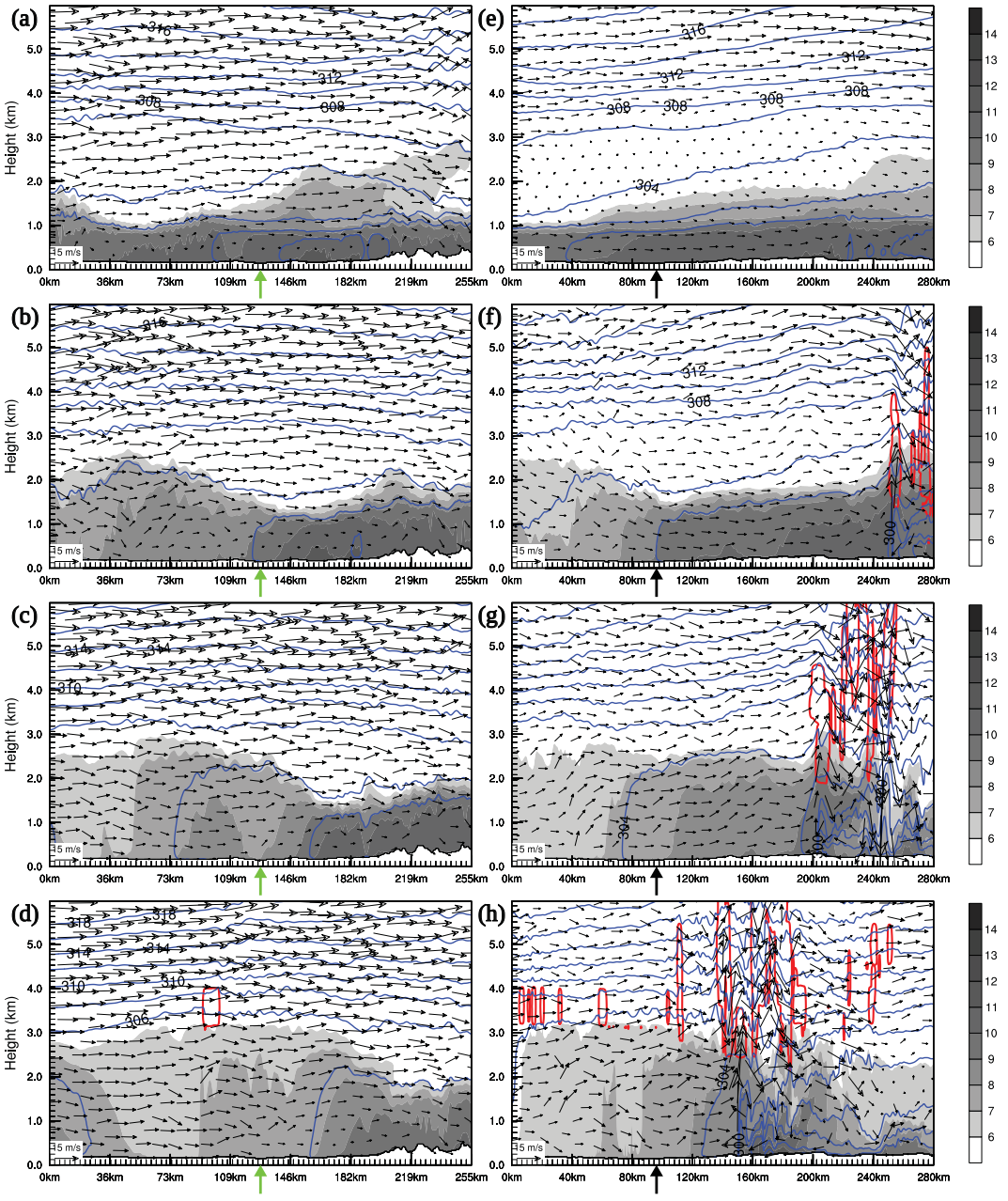

FIG. 8. Water vapor mixing ratio q_v (gray shading; g kg^{-1}), potential temperature (blue contours; K), the 0.01 g kg^{-1} total water–ice condensate contours outlining the cloud (red contours), and wind vectors (m s^{-1}), in the cross sections denoted by the black lines in Fig. 7 at (a) 1030, (b) 1230, (c) 1330, and (d) 1500 LST. (e)–(h) As in (a)–(d), but for the green lines in Fig. 7. The left and right cross sections in the same row are perpendicular to each other at the same time, with the intersection denoted by the green and black arrows, respectively.

(Fig. 7b). Deep convective clouds are found above the cold pool north of the gust front (at ~200 km; Fig. 8g) as the front pushes southward. By 1500 LST, the southern half of the cross section is located west of the dryline (Fig. 7c), while new shallow clouds have formed in the 3–4-km layer above deepened mixed CBL in this portion (Fig. 8h). As is seen in Fig. 9, this 3–4-km layer corresponds to relative humidity (RH) above 90% (Figs. 9g,h), while the RH in the CBL below is less than 40%. The RH in the 3–4-km layer has increased steadily over the proceeding hours (Fig. 9), most likely due to moisture advection by southerly flows at these levels. The nearly saturated layer in terms of high RH provides favorable conditions for cloud formation and suggests that the clouds ahead of the gust front form at elevated levels above a relatively dry CBL.

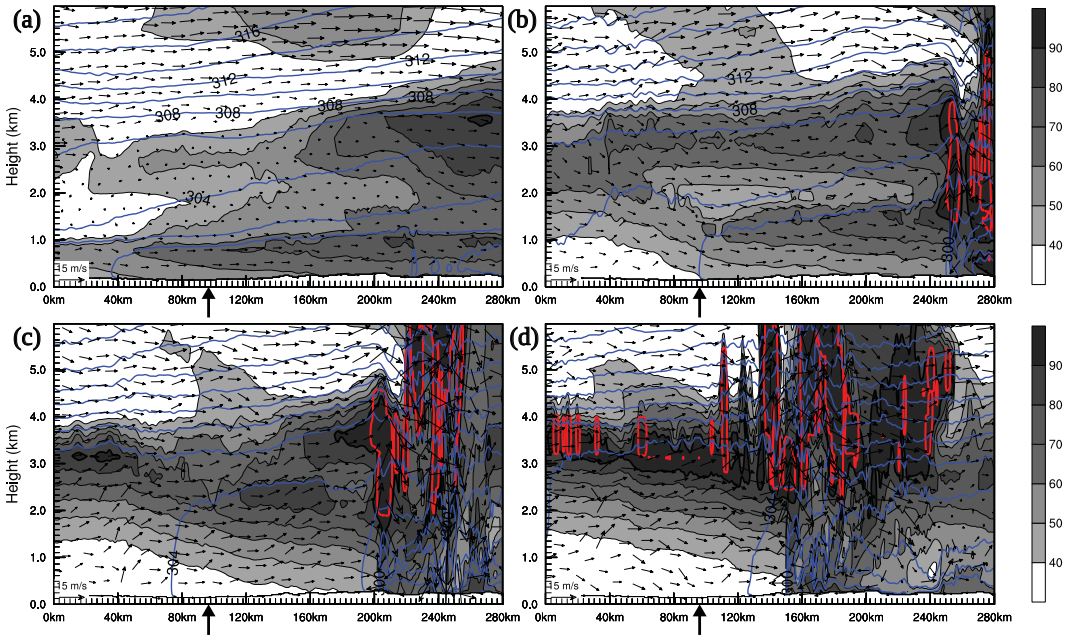

FIG. 9. As in Figs. 8e–h, but the gray shading is for RH.

c. *The role of convectively generated GWs*

While the moist layer above the CBL can provide favorable conditions for CI, clouds first form at specific locations within the layer (Figs. 8h and 9d), suggesting the presence of localized forcing there. The model-simulated vertical velocity fields at 4 km MSL together with the 2.75 km MSL contours of 0.01 g kg^{-1} total water–ice condensate outlining the cloud are shown in Fig. 10 to investigate such localized forcing. The choice of these heights is based on the fact that the GW amplitudes are largest at ~4-km height and the clouds first form at ~2.75 km (see later).

At 1400 LST, the convection becomes mostly concentrated behind the spreading gust front. Ahead of the gust front, there are trains of high-frequency short-wavelength GWs, in the form of updraft–downdraft couplets extending to the southwest (see the red box in Fig. 10). Such short-wavelength, high-frequency nonhydrostatic GWs have been shown to be generated by frequent temporal changes in the heating profile associated with multicellular development within a convective line and require a wave duct to maintain their strength at the lower troposphere (Fovell et al. 2006).

As the high-frequency GWs emanate from the MCS convection behind the gust front, a series of short cloud bands are generated in phase with the wave peaks and along the wave propagation path ahead of the gust front (in the red box in Fig. 10). This wavelike banded pattern is consistent with what is observed by *FY-4A* satellite (in red boxes in Fig. 3), and similar patterns have been documented in previous studies (Du and Zhang 2019; Lane and Zhang 2011; Raymond 1987). It should be noted that the simulated wave bands are oriented east-northeast–west-southwest, which is somewhat different from the observed northwest–southeast orientation (Fig. 3). This may be attributed to the differences in the detailed convective structures between the simulated and observed MCSs.

To lend support to the simulated environment in which the GWs and initial cloud bands form, we looked for observed soundings in the region. The only sounding station that is

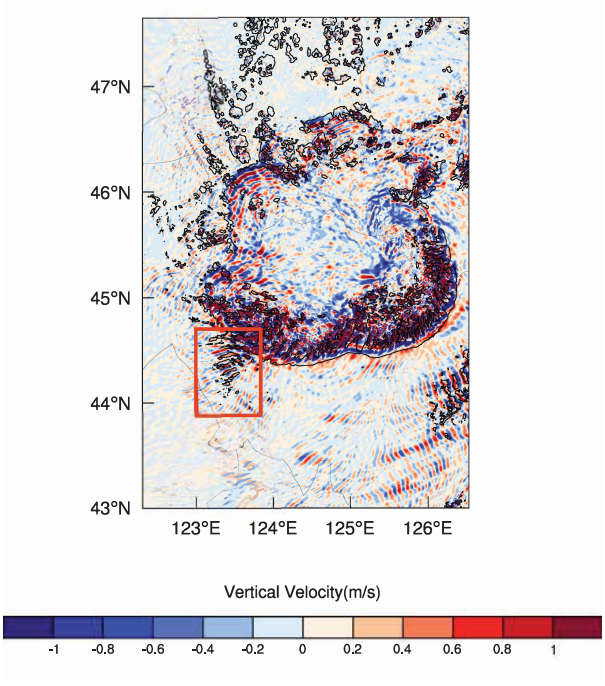

FIG. 10. Model-simulated 4 km MSL vertical velocity (color shading; m s^{-1}) and the 2.75 km MSL 0.01 g kg^{-1} total water–ice condensate contours outlining the clouds (black contours) at 1400 LST.

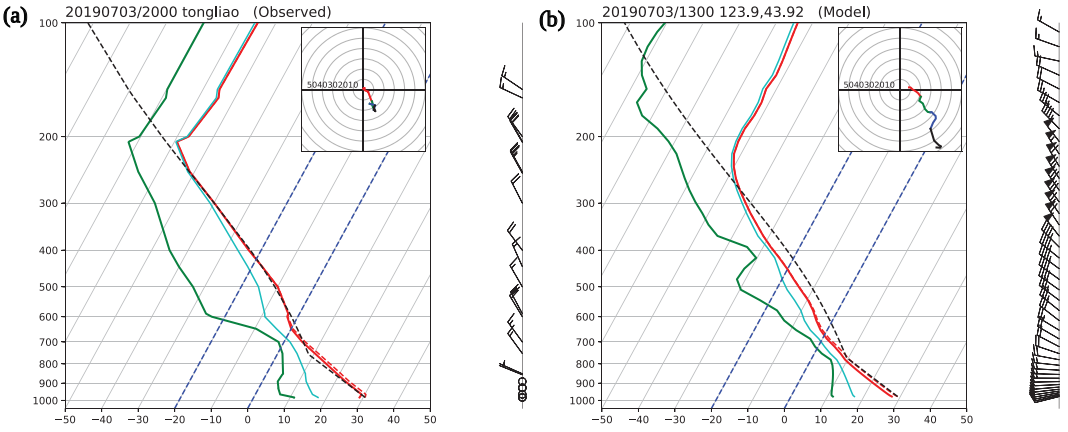

FIG. 11. Skew *T*–log*p* diagrams of sounding (a) observed at Tongliao station at 2000 LST 3 Jul 2019 (see white star in Fig. 3a) and (b) extracted from model simulation at the black star location in Fig. 6d at 1300 LST 3 Jul 2019.

close enough to the cloud bands is that of Tongliao, located at the white star location in Fig. 3a. However, the sounding is available at either 0800 LST or 2000 LST. The 0800 LST early morning sounding is not representative of the afternoon condition when the cloud bands form. The 2000 LST sounding, although much later than the time of cloud band formation, may still show some characteristics of the afternoon boundary layer and structure above. A model sounding is extracted from the simulation near the CI location at 1300 LST (see the black star in Fig. 6d). This location is ahead of the MCS gust front and west of the surface dryline within the westerly flow (Fig. 6d), while the Tongliao sounding should also be located west of the dryline. The 2000 LST Tongliao sounding and the model-extracted 1300 LST sounding are plotted in Fig. 11.

Overall, the observed and simulated vertical profiles have similar low-level structures. They both have a stable layer with higher relative humidity above the well-mixed CBL, with the stable layer in the observed sounding being somewhat higher in elevation, likely due to additional late afternoon CBL mixing. The stable layer would support horizontally propagating GWs, and the high relative humidity makes it easier for saturation to occur, leading to cloud formation and CI. We want to point out that, being located west of the dryline with surface winds being mostly westerly, these soundings do not represent the conditions of inflow that feed the later intensification of convective cell into the tornadic supercell. The intensification does not happen until the cell growing out of the initial cloud bands moves to the east of the dryline where the boundary layer air is much more moist and the low-level flow is from the southwest (compare Fig. 6d). The observed sounding has little CAPE (likely because the sounding location was further west relative to the dryline by 2000 LST), while the extracted model sounding has moderate CAPE that can support the initial development of convection.

To examine the detailed evolution of the high-frequency GWs and their associated cloud bands to the southwest, an enlarged view of the region in the red box in Fig. 10 is shown in Fig. 12. For simplicity, the peak updraft (positive w) regions of GWs are marked by dashed lines labeled U1 to U9, while their associated cloud bands are labeled C1 to C9. The straight black lines labeled A1–A2 in Fig. 12 indicate the locations of vertical cross sections in Figs. 13 and 16 and are chosen to go through the main high-frequency GW bands. The cross sections are shifted eastward to follow the GWs and to examine the evolution of waves and the formation of the cloud bands.

The banded structures are clearly identifiable at 1350 LST (Fig. 12a). The updraft bands are well defined, and the associated clouds exhibit more scattered features as they have just formed at the time. Afterward, the corresponding cloud bands grow more or less in phase with the peak updraft regions. As a result, the clouds become much wider and well organized (Figs. 12b,c). Overall, new updraft and cloud bands continue to form on the south side of the wave train between 1408 and 1424 LST (Figs. 12d–f). This results in effective south-southeastward propagation of the GW train. The patterns of the GWs and cloud bands in the vertical cross sections are consistent with those observed in the horizontal planes (Fig. 13). In addition, the updraft–downdraft couplets of the GWs are mostly located between 2- and 6-km height above the CBL, with the peak intensities located at ~4 km.

One noteworthy feature seen from the pattern is that the clouds tend to form and develop on the downwind side of the updrafts where ascent reaches maximum (see C4 in Fig. 12a and C9 in Fig. 12e), which is more evident in the vertical cross sections (see C3 and C4 in Fig. 13a). Furthermore, a quarter of a phase difference can be observed between the potential temperature perturbation and vertical velocity fields (Fig. 13). Such a pattern has also been noted by Fovell et al. (2006), who explain that in forward-propagating GWs, the wave-relative flow is directed toward the storm, and parcels experience the longest period of upward forcing by updrafts right before they enter the downdraft regions. As a result, CI tends to occur on the downwind side of the wave crest/updraft (see Fig. 11 in their paper). Despite the ground-relative wave speed being slower in our case, the intrinsic phase speed remains significant when we count the strong storm-relative winds above the CBL (Fig. 13).

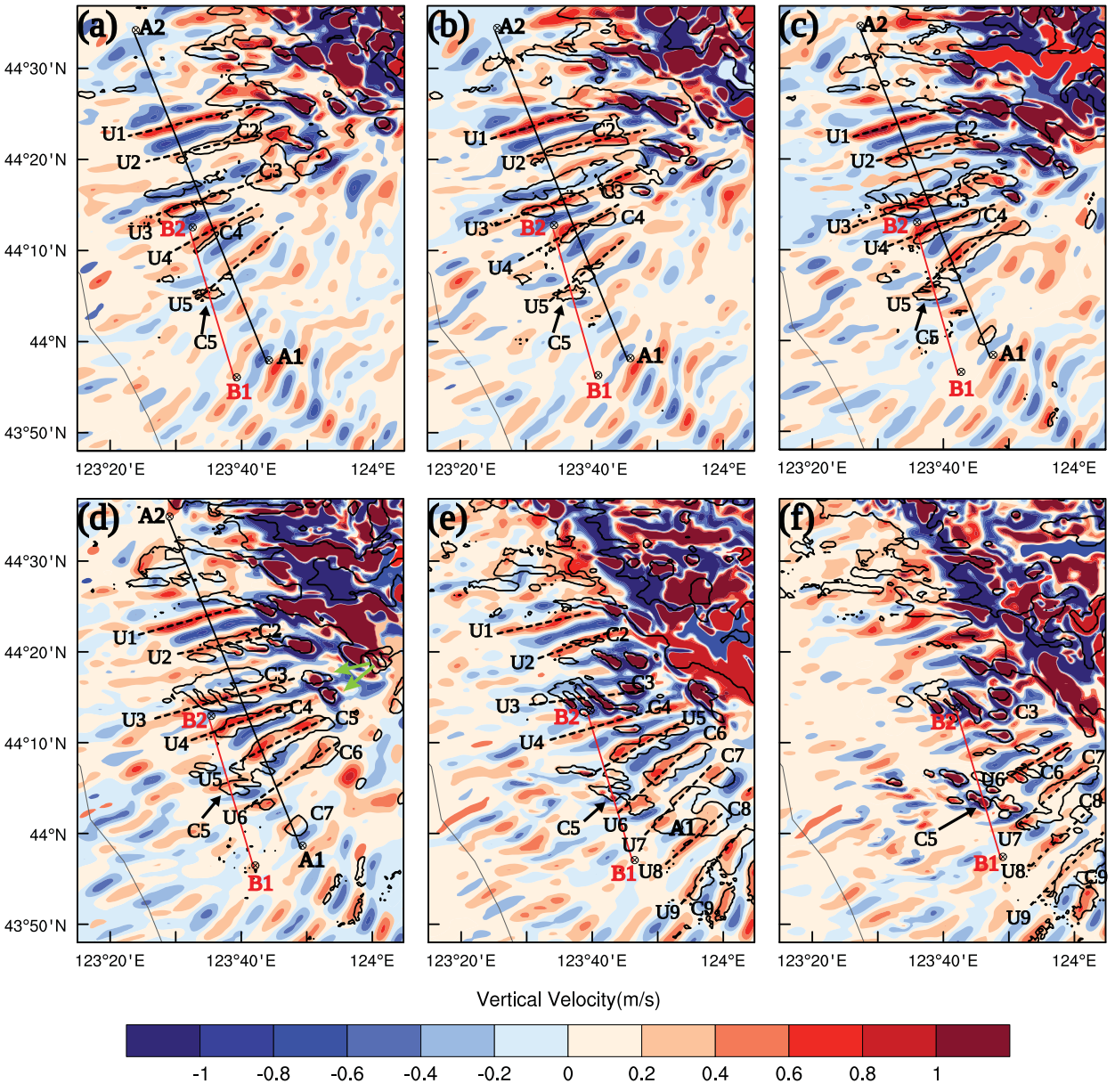

FIG. 12. Model-simulated 4 km MSL vertical velocity (color shading; m s^{-1}) and the 2.75 km MSL 0.005 g kg^{-1} total water–ice condensate contours outlining the clouds (black contours) in the zoomed-in region indicated by the red box in Fig. 10 at (a) 1350, (b) 1354, (c) 1402, (d) 1408, (e) 1418, and (f) 1424 LST. The black straight lines A1–A2 indicate the locations of vertical cross sections shown in Figs. 13 and 16. Red straight lines B1–B2 indicate the locations of vertical cross sections shown in Fig. 14. The upward branches of GWs are marked by straight dashed lines and labeled U1 through U9. Labels C1 through C9 refer to cloud bands shown by black contours associated with U1 through U9. Two cells that evolved from C3 and C4 are highlighted by green arrows.

It should also be noted that only a few cells develop into DMC in the end, although a number of cloud bands are produced by the GWs. The merger of initial cells into the MCS before they could fully develop is a major reason responsible for the failure of those cells to develop into mature, isolated DMC. For instance, C2 develops quite well during the initial stages (Figs. 12a–c and 13a,b), but it is advected toward and merges with the MCS before it can fully develop (Figs. 12e,f). This behavior also occurs in C3 and C4 (see the two cells pointed to by green arrows in Fig. 12d, and they are ingested into the MCS and disappear in Fig. 12e). The same reason was found to be responsible for the reinvigoration of the squall lines by Fovell et al. (2006). In their study, the newly formed clouds generated by GWs ahead of the squall line are then advected to the main system by the storm-relative wind.

To carefully examine the initiation of the supercell, vertical cross sections (B1–B2 lines in Figs. 12 and 15) following cell C5 that subsequently evolves into the tornadic supercell are

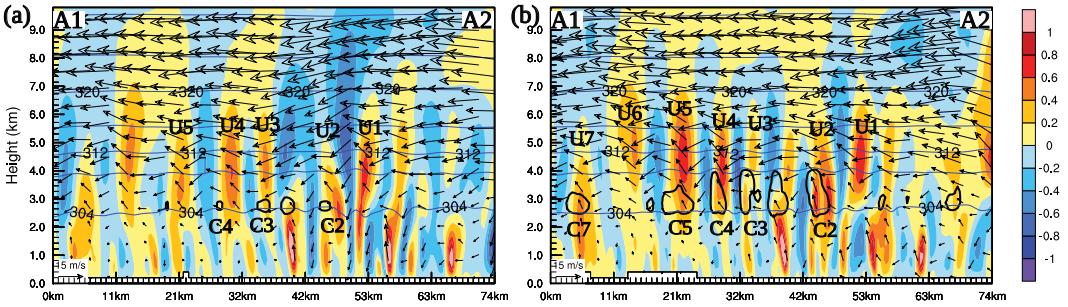

FIG. 13. Vertical velocity (color shading; m s^{-1}), potential temperature (dark blue contours; K), the 0.01 g kg^{-1} total water–ice condensate contours (thick black contours), and storm-relative wind vectors (m s^{-1}), in the cross sections denoted by the black lines A1–A2 in Fig. 12 at (a) 1350 and (b) 1408 LST.

shown in Fig. 14. The B1–B2 lines move from west to east with a speed of 8.3 m s^{-1}. The initial cloud associated with cell C5 first forms in the elevated moist layer above the CBL at about 1350 LST near the wave crest (Fig. 14a). During its initial stages, the development of C5 appears to be additionally supported by an updraft that is located within the CBL and underneath the U5 (Figs. 14a,b). Taking a close look at the horizontal convergence fields near the ground, we find that this CBL updraft is actually the upward branch of the circulations of a horizontal convective roll (HCR; pointed by the blue arrows in Fig. 15). This HCR updraft is collocated with the western end of U5 during the initial stage of C5 (Figs. 15a–f) so that the upward motion extends from surface to midtroposphere (Figs. 14a,b). It should be noted that this initial stage takes about 20 min (Figs. 14a,b).

Previous studies have shown the interaction of HCRs with a dryline can provide favorable localized forcings for CI (Edwards et al. 2000; Wang and Xue 2012, 2018; Xue and Martin 2006a,b). Different from these studies, the additional lifting by the HCR updraft underneath the higher-level GW updraft appears to promote faster growth of C5 in our case. However, not all clouds are supported by the boundary layer HCRs. For instance, C4 is formed on the downwind side of U4, and there is no HCR updraft under it (Fig. 15c); it grows more slowly (Figs. 15d–f). This is also the case for the eastern part of U5 where the clouds form more slowly compared to those on its western end (Figs. 15d–f). In general, the banded clouds form first along with the peak updrafts of above-CBL GWs rather than CBL HCRs, but their growth can be assisted by the presence of HCR updrafts directly underneath.

After the initial stage, the updraft core of C5 is established and is advected southward by the stronger storm-relative wind aloft, detached from the CBL updraft below, and actually into the downdraft region of GW (Figs. 14c–f). However, it continues to grow in depth and intensity and apparently becomes self-sustained by its condensational heating which is enough to overcome the downward motion of GW (Figs. 14f,g). The cloud top reaches 5-km height, and C5 becomes clearly the dominant convective cell (Figs. 14e–h). At 1424 LST (Fig. 14g), the updraft of C5 has extended below the moist layer into the CBL, which appears to have been aided by the CBL upward motion underneath. By 1428 LST (Fig. 14h), the updraft of C5 had extended to below 1 km above ground level (AGL), apparently drawing CBL air into the deep convection that has been established, even though the CBL air has lower RH (but higher q_v). The nearly neutral stratification of the CBL (compare Fig. 8) makes the air easy to draw into the deep clouds above (Fig. 14h). Eventually, C5 develops into a DMC and gains supercell characteristics in subsequent hours (Fig. 6f).

d. Trapping mechanism of the GWs

In the last section, we showed that high-frequency GWs propagating along the stable layer above the CBL trigger the convective cell that eventually develops into the tornadic supercell. In this section, we examine the conditions favorable for GW propagation in the layer. As mentioned earlier in the introduction, high-frequency GWs excited at the lower levels of the atmosphere tend to propagate vertically, losing their energy to the higher levels unless a trapping mechanism is present (Alexander and Holton 2004; Fovell et al. 1992; Nicholls et al. 1991). In Fovell et al. (2006), trapping was produced by the curvature of the vertical wind profile due to a forward anvil outflow that created a trapping level at about 7-km height. Not being able to radiate energy upward, the GWs would then mainly propagate horizontally and be able to reach a large distance sometimes.

The parameter that best describes the conditions for vertical GW propagation is the Scorer parameter l^2 which is a function of the static stability and vertical variation of the wind profile. According to GW analytical solutions, GWs whose wavenumbers are larger than the Scorer parameter cannot propagate vertically (Crook 1988; Scorer 1949). When the Scorer parameter l^2 decreases with height, GWs of certain wavelengths will cease to propagate upward when the Scorer parameter value falls below their wavenumbers, causing the trapping of the waves. Such waves tend to propagate horizontally if a suitable stable condition exists, and such a stable layer acts as a "waveguide."

The Scorer parameter l^2 can be calculated according to

$$l^2 = \frac{N_m^2}{(U-c)^2} - \frac{\partial^2 U/\partial z^2}{(U-c)}, \tag{1}$$

where $U(z)$ is the environmental horizontal wind profile, z is the height, and c is the horizontal GW phase speed. The term N_m^2 is the subsaturated or saturated Brunt–Väisälä frequency as defined in Bryan and Rotunno (2009). The Scorer parameter l^2

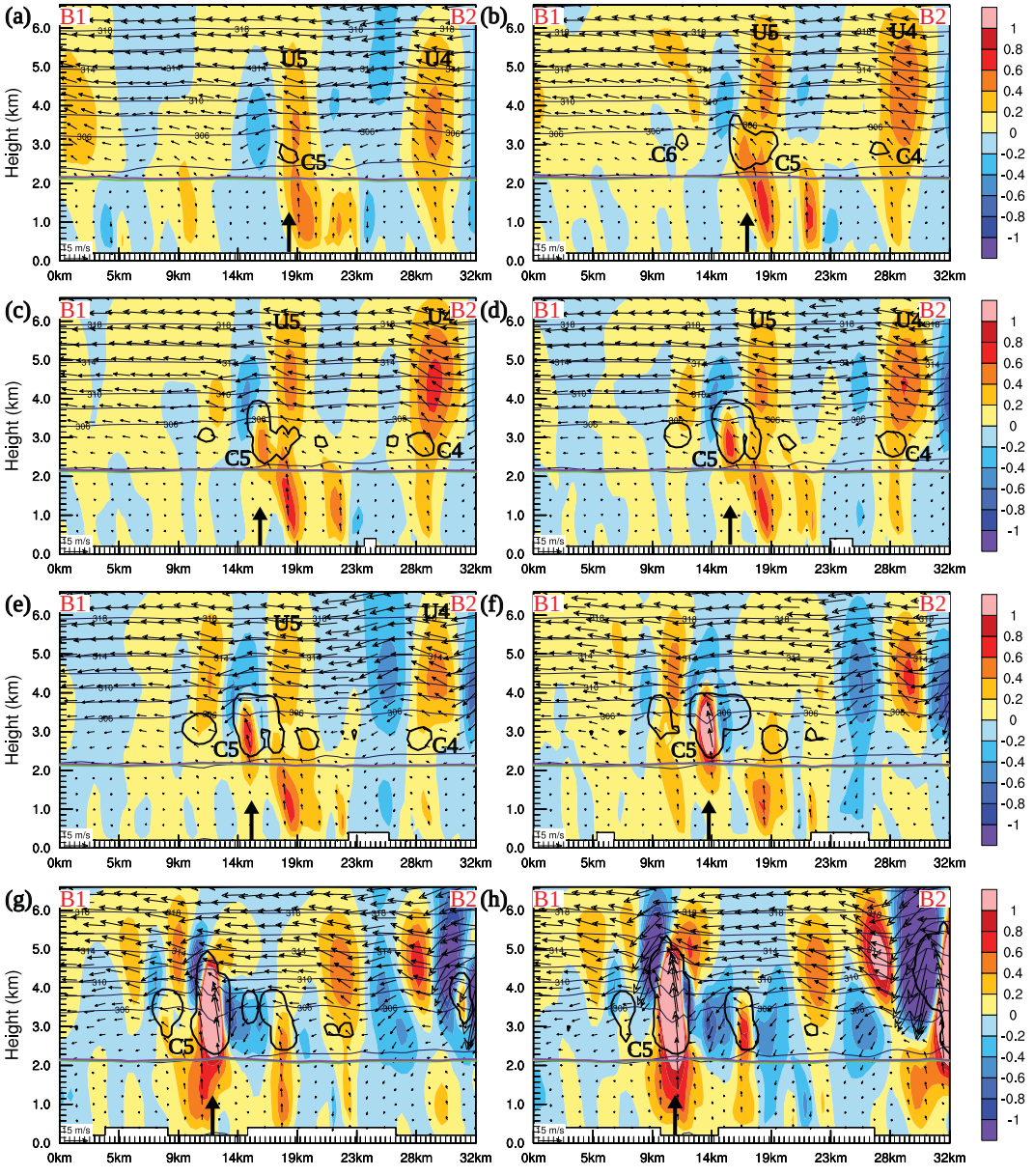

FIG. 14. Vertical velocity (color shading; m s^{-1}), potential temperature (dark blue contours; K), the 0.01 g kg^{-1} total water–ice condensate contours (thick black contours), LCL (green contours), LFC (purple contours), and storm-relative wind vectors (m s^{-1}), in the cross sections denoted by red lines B1–B2 in Fig. 12 at (a) 1350, (b) 1408, (c) 1410, (d) 1412, (e) 1414, (f) 1418, (g) 1424, and (h) 1428 LST. The black arrows point to the initial cell that evolves into the tornadic supercell.

will decrease when static stability N_m^2 decreases, U increases, or $\partial^2 U/\partial z^2$ is large and negative at lower altitudes but small at higher altitudes.

For saturated air,

$$N_m^2 = \frac{g}{T}\left(\frac{\partial T}{\partial z} + \Gamma_m\right)\left(1 + \frac{T}{R_d/R_v + q_s}\frac{\partial q_s}{\partial T}\right) - \frac{g}{1+q_t}\frac{\partial q_t}{\partial z}, \quad (2)$$

where g is the gravitational acceleration, T is the absolute temperature, Γ_m is the moist-adiabatic lapse rate, R_d is the gas constant for dry air, R_v is the gas constant for water vapor, q_s is the mixing ratio at saturated equilibrium, and q_t is the total water mixing ratio. The term c is usually calculated as the average ground-relative GW phase speed. We estimate the phase speed by dividing the distance traveled by GWs with their traveled time, giving us an estimated ground-relative wave speed of 9.7 m s^{-1}.

According to (1), we calculate l^2 as well as its separate terms:

$$l_N^2 = \frac{N_m^2}{(U-c)^2}, \quad (3)$$

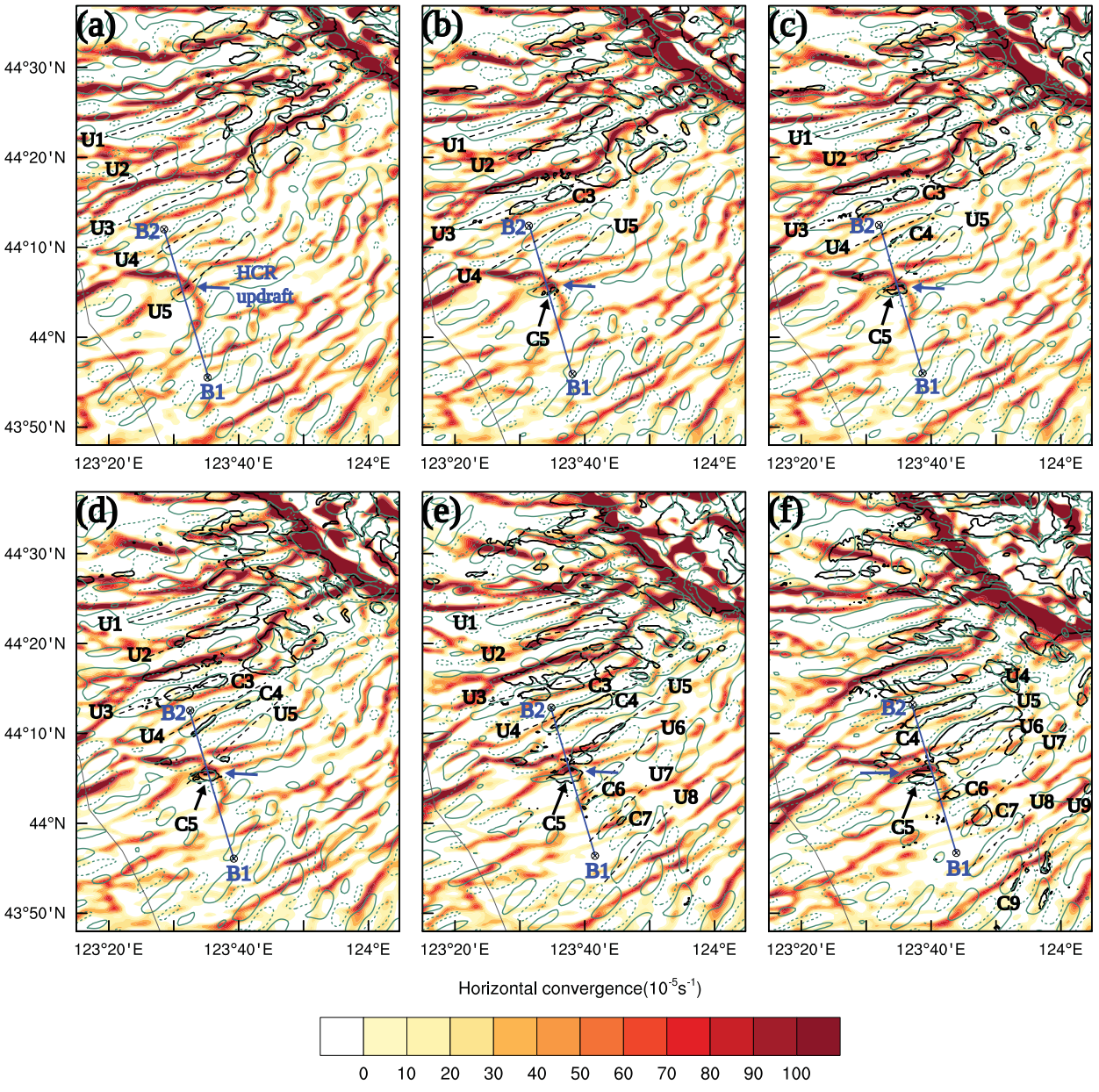

FIG. 15. Horizontal convergence fields at the first model level (color shading; 1×10^{-5} s^{-1}), the vertical velocity at 4 km MSL (green contours; ± 0.2 m s^{-1}), and the 2.75 km MSL 0.005 g kg^{-1} total water–ice condensate contours outlining the clouds (black contours) in the zoomed-in region indicated by the red box in Fig. 10 at (a) 1336, (b) 1346, (c) 1348, (d) 1350, (e) 1358, and (f) 1406 LST. The upward branches of GWs are marked by straight dashed lines and labeled U1 through U9. Labels C1 through C9 refer to cloud bands shown by black contours associated with U1 through U9. The HCR updraft, which keeps supporting the initiation of C5, is pointed to by the blue arrows. Blue straight lines B1–B2 indicate the locations of vertical cross sections shown in Fig. 14.

and

$$l_s^2 = -\frac{\partial^2 U/\partial z^2}{(U-c)}, \tag{4}$$

which are related to environment stability and the curvature of the wind profile, respectively.

Figure 16 shows Scorer parameter l^2 and their separated terms in a vertical cross section alone A1–A2 at 1408 LST in Fig. 12d. Their values are multiplied by 10^6 for plotting. Also shown are the 0.01 g kg^{-1} total liquid–ice condensate contours outlining the clouds. For the Scorer parameter l^2 in Fig. 16a, the most evident feature is a layer between 6 and 7 km where l^2 is negative. For a wave with horizontal wavelength L_x and wavenumber $k = (2\pi/L_x)$, the vertical wave energy propagation can only occur when $l^2 > k^2$; otherwise, the wave will be vertically decaying so that the energy is trapped

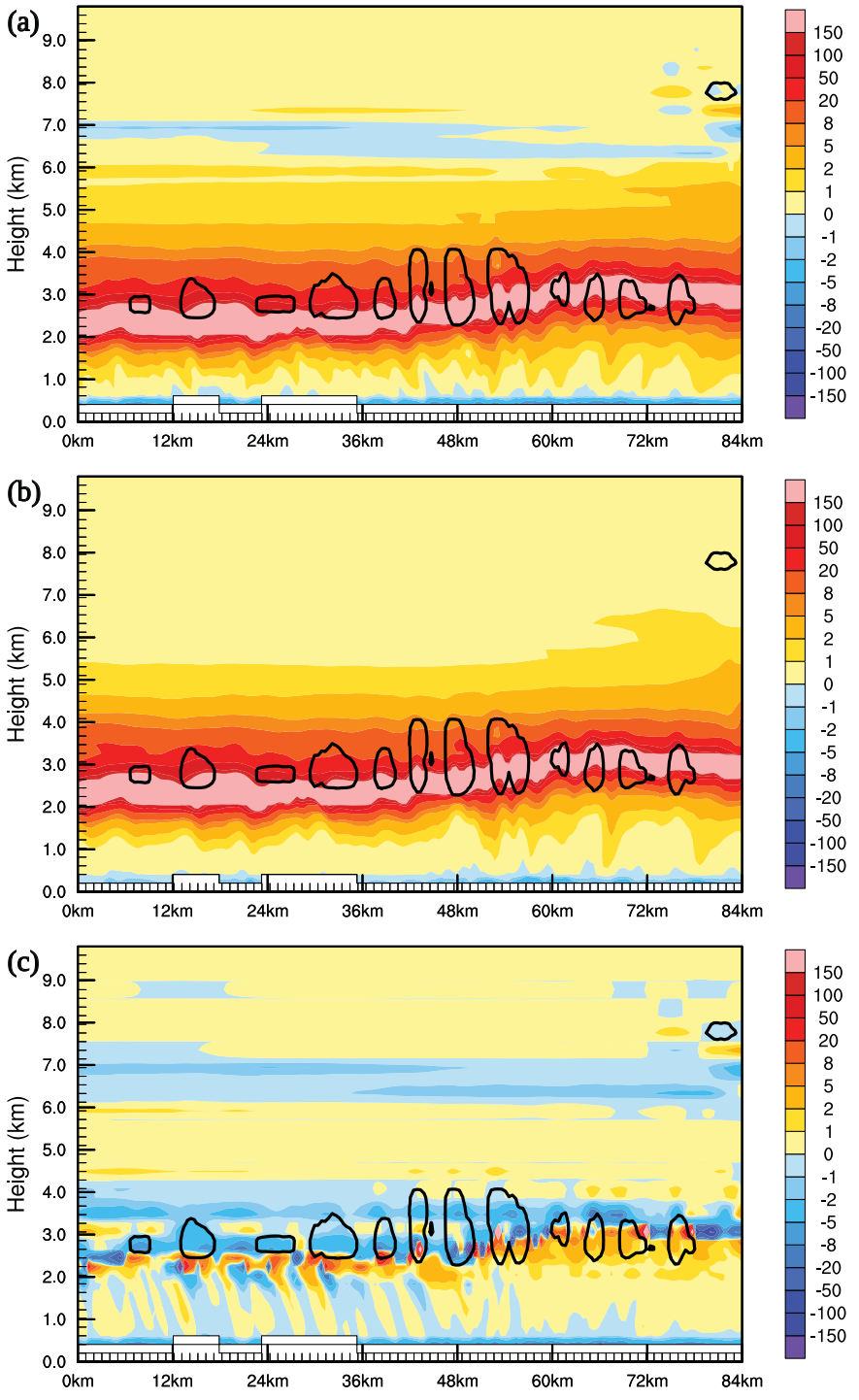

FIG. 16. (a) Scorer parameter (color shading; 1×10^{-6} m^{-2}) and the 0.01 g kg^{-1} total liquid–ice condensate contours (thick black contours) in the cross sections denoted by the black lines A1–A2 in Fig. 12 at 1408 LST. (b),(c) As in (a), but for the terms associated with environment stability and the curvature of the wind profile, respectively.

and can only propagate horizontally (Crook 1988). From vertical cross sections we discussed earlier, we can obtain an estimated wavelength of GWs of 6 km (Fig. 13), which gives us a wavenumber k of 10^{-3} and k^2 of 10^{-6}. Based on the wave propagation theory, when l^2 is less than 10^{-6} in a layer, no GW can propagate vertically through this layer, and all GW energy will be trapped below this layer, helping maintain the amplitudes of GWs below. Indeed, none of the GW updrafts

reaches above the 7-km height where l^2 is negative (Fig. 13). The term l^2 is the largest between ~2 and ~4 km and decreases above and below this layer. The smaller l^2 overlying large values also cause the trapping of shorter wavelength GWs when they try to propagate upward and encounter reduced l^2. The 2–4-km layer is one that is most favorable for supporting GWs, and it acts as a waveguide along which larger-amplitude GWs propagate horizontally, reaching distances ahead of the source regions behind the gust front. This is supported by the fact that the GW amplitudes start to decrease at 4-km height (Fig. 13).

An examination of the total l^2 and contribution terms reveals that the layer of large positive l^2 is mainly attributed to the stability term, while the negative l^2 is mainly from the wind profile curvature (Fig. 16). Although there is another evident negative l^2 layer for the term associated with wind profile curvature between ~2- and ~4-km levels, it is overwhelmed by the large positive stability term.

In summary, a stable layer with large positive Scorer parameter values above the CBL provides favorable conditions for the GWs excited by nearby intense convection along the MCS gust front to propagate horizontally along the waveguide, while decreasing the Scorer parameter above and below this layer, and a layer of negative values in the upper troposphere helps trap the GW energy to this layer and maintain significant amplitudes. With high relative humidity in this stable layer, air parcels within the large amplitude GW updrafts are easy to reach saturation and their level of free convection and trigger deep convection. When a GW updraft with a developing cloud cell within is over the upward branch of a boundary layer convective circulation, the cell strengthens faster than others. When the updraft core becomes self-sustained and starts to draw nearly neutrally stratified CBL air into its core, deep convection is established, which eventually evolves into the tornadic supercell in our case.

5. Summary and conceptual model

This study investigates the CI mechanism of a tornadic supercell that occurred in Kaiyuan City, Liaoning Province, China, on 3 July 2019. This event and certain features are first documented using high-resolution observations including *FY-4A* visible satellite data, Doppler radar data, and data from automatic weather stations. The presence of wavelike cloud bands ahead of the gust front of an MCS and the development of the tornadic supercell from one of the fastest-growing cloud cells along the bands suggest a potentially important role of convection-excited gravity waves in triggering the supercell convection. A nested-grid, high-resolution numerical simulation is performed to investigate the CI processes. The simulation results show a reasonable agreement with the observations despite timing and spatial errors and discrepancies in smaller-scale details. The general evolution of the predicted MCS is consistent with the observation, and the initial cell of the tornadic supercell in the model also initiates ahead of the gust front as in observations. A detailed investigation of the simulation results reveals that the initial cells are triggered on the dry side of a surface dryline and within a moist stable layer above a well-mixed CBL that is relatively dry, especially in terms of RH. The moist stable layer is almost saturated and provides favorable conditions for gravity wave propagation in the layer. The near-saturation condition makes it easy for air parcels to be lifted above their LFC.

Clouds first form at specific locations within the moist layer, and analyses show that high-frequency GWs provide the primary localized lifting for the cloud formation and triggering of deep convection within our simulation. These GWs are generated by the cyclical redevelopment of convection within the MCS and propagate southward along the stable layer which acts as a waveguide above CBL. A quarter of the phase difference exists between the vertical velocity and potential temperature perturbations confirming the GW nature, and the clouds tend to form on the downwind side of the GW updrafts where the vertical ascent is maximized. While a train of cloud bands forms near the peak updrafts of the GWs, only a few cells develop into deep convection. Some of the cells are advected toward and end up merging with the MCS.

Examination of vertical cross sections reveals additional interactions with updrafts of convective cells within the CBL below. The CBL convective cells organize into HCRs and produce localized bands of updraft. The cloud cell that eventually developed into the supercell first formed in the moist stable layer and appears to be helped by the updraft of an HCR directly underneath, making this cloud cell grow faster than surrounding cells and become the dominant one. As this cell grows deeper and more intense, condensational heating makes its updraft self-sustained. It then moves away from the initial GW wave crest (updraft region) into a wave trough (downdraft region), as well as away from the HCR updraft originally underneath, but is still able to maintain its growth. When the cell moves into the next GW wave crest region that also has a CBL updraft nearby, it rapidly intensifies and forms deep convection. After that, the storm cell starts to draw air from the boundary layer below, which has higher q_v and is nearly neutrally stratified. Eventually, the storm cell moves eastward to the moist side of the dryline where it eventually evolves into an isolated supercell.

The trapping conditions for GWs are analyzed by examining the vertical structure of the Scorer parameter. The Scorer parameter is positive and the largest in the stable layer above the CBL and decreases both above and below this layer, preventing certain shorter-wavelength GWs from propagating vertically away from the stable layer, especially in the upward direction in which the GW energy tends to radiate. Further, there exists a layer of negative Scorer parameter in the upper troposphere due to wind shear, so that no lower-level GW can penetrate it to reach the upper levels. Such vertical structures create trapping conditions for GWs and an effective waveguide along which GWs can propagate horizontally to relatively large distances from their sources.

Based on the above findings, we propose a conceptual model of the initiation mechanism of the tornadic supercell in this case which includes a schematic illustrating the trapping mechanism of the high-frequency GWs and their roles in initiating cloud cells and the development of some cells into deep convection (Fig. 17). Specifically, at the development stage of

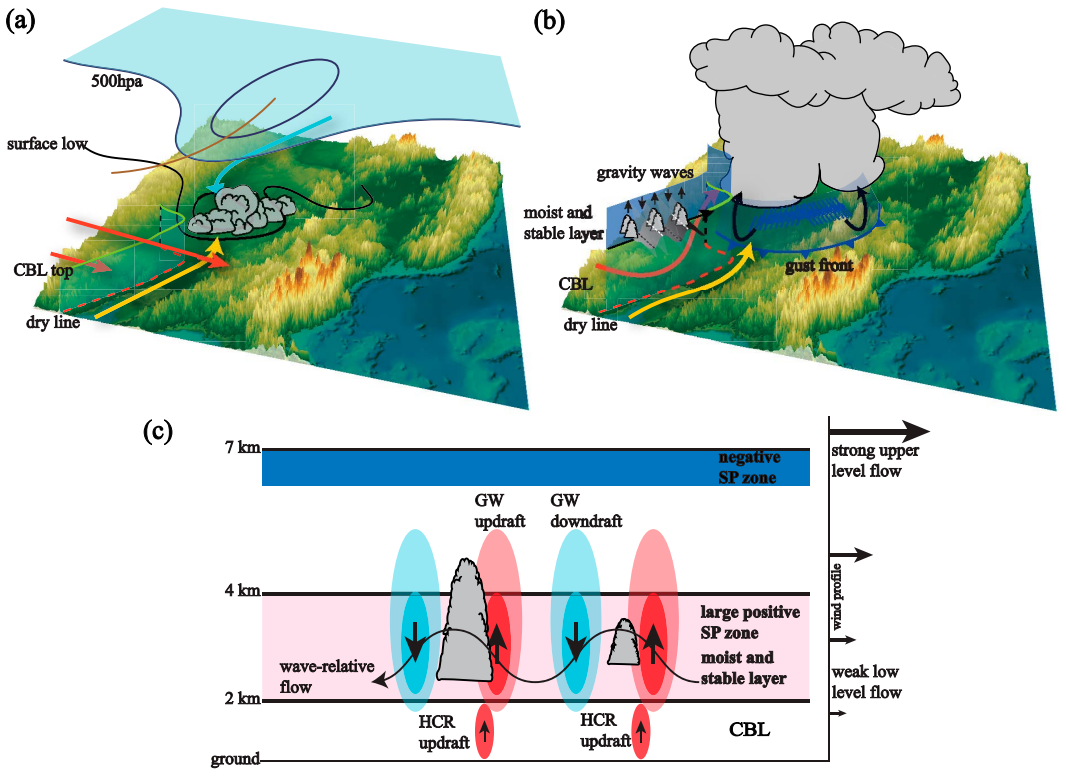

FIG. 17. A conceptual model of the initiation of the tornadic supercell in the 3 Jul 2019 Kaiyuan, Liaoning, tornado case. (a) The development stage of a presupercell MCS, including the surface low with the North China cold vortex (dark blue contours and transparent sky-blue shading), the dryline (red dashed line), the moist southwesterly flow (curved yellow arrow), the dry westerly flow (red arrow), and the CBL top (green line). (b) The CI stage of the supercell, including the convectively generated GWs (gray wavy shading), the moist stable layer (blue shading) above the CBL (green shading), and the MCS gust front (blue front symbol). (c) Schematic illustrating the trapping mechanism of the high-frequency GWs and their roles in producing cloud cells, including the layer of negative Scorer parameter (shaded dark blue), the moist and stable layer with the largest positive Scorer parameter (shaded pink), the wave-relative flow (the long wavy arrow), the updrafts of HCRs (red elliptic shading in the CBL), the GW updrafts and downdrafts (red and blue elliptic shading), and wind profile.

a presupercell MCS (Fig. 17a), the MCS forms on a surface low with a North China cold vortex at the mid- and upper levels. A dryline with strong moisture contrast extends from ahead of the surface low southwestward along the Bohai Bay coastal line. The moist southwesterly flow from Bohai Bay to the east of the dryline brings moist air to the MCS, while the dry westerly flow west of the dryline originates from the Greater Khingan Range and Mongolian Plateau. At the convective initiation stage of the supercell (Fig. 17b), initial cloud cells are triggered by the convectively generated GWs that propagate southward and away from the MCS along a moist, in terms of high relative humidity, stable layer above the CBL ahead of the MCS gust front that acts as a waveguide for the GWs. In the schematic (Fig. 17c), a layer of negative Scorer parameter exists at around the 7-km level, through which no low-level GWs can penetrate. The moist and stable layer above the CBL has the largest positive Scorer parameter and its value decreases with height, which will trap shorter-wavelength GWs to the large Scorer parameter layer. The wave-relative flow is indicated by the long wavy arrow with the initial clouds forming on the wave crests. The faster growth of the initial cloud cell that eventually becomes the dominant deep convection is helped by the updraft within the boundary layer located below, associated with boundary layer convective cells that are mostly organized into HCRs.

While earlier studies, mostly based on idealized numerical simulations, have documented the initiation of new convective cells by low-level horizontally propagating GWs triggered by intense organized convection, studies documenting similar processes for real cases are few. Improved understanding of elevated convective initiation involving convectively generated GWs should be valuable to operational forecasting, as there is often no clear forcing at the surface. The analyses we performed on the convective initiation and evolution, including the role of convectively generated GWs in triggering the initial convective cell that evolves into the supercell thunderstorm, are mainly based on model-simulated results. While direct observations on perturbations associated with the GWs are not available, the cloud bands in visible satellite images suggest the presence of GWs in the region. The overall

similarity in system structure and timing between observations and models also suggests that the proposed GW mechanism might have played a crucial role in the genesis of the actual Kaiyuan tornadic supercell. Future studies involving more fine-scale observations should be carried out for similar cases that hopefully can provide direct observational evidence of such an initiation mechanism. Studies should also be carried out to determine how often such processes occur in different seasons and environmental regimes.

Acknowledgments. This work was primarily supported by NSFC Grant 41730965.

Data availability statement. NCEP 0.25° GDAS/FNL analysis data and GFS 0.25° analysis and forecast data can be downloaded online (rda.ucar.edu/lookfordata/datasets/?nb=y&b=topic&v=). The *FY-4A* satellite dataset can be downloaded online (https://data.cma.cn/). Radar data and automatic weather station (AWS) data are provided by the Liaoning Meteorological Bureau, Jilin Meteorological Service, and Heilongjiang Meteorological Bureau. The processed datasets within this paper, including the radar, satellite, AWS, NCEP 0.25° GFS analysis and forecast datasets, NCEP 0.25° GDAS/FNL analysis datasets, and numerical simulation outputs, can be found at Harvard Dataverse (https://doi.org/10.7910/DVN/XCU0TA).

REFERENCES

Adams-Selin, R. D., 2020: Impact of convectively generated low-frequency gravity waves on evolution of mesoscale convective systems. *J. Atmos. Sci.*, **77**, 3441–3460, https://doi.org/10.1175/JAS-D-19-0250.1.

——, and R. H. Johnson, 2013: Examination of gravity waves associated with the 13 March 2003 bow echo. *Mon. Wea. Rev.*, **141**, 3735–3756, https://doi.org/10.1175/MWR-D-12-00343.1.

Alexander, M. J., and J. R. Holton, 2004: On the spectrum of vertically propagating gravity waves generated by a transient heat source. *Atmos. Chem. Phys.*, **4**, 923–932, https://doi.org/10.5194/acp-4-923-2004.

Bai, L., Z. Meng, Y. Huang, Y. Zhang, S. Niu, and T. Su, 2019: Convection initiation resulting from the interaction between a quasi-stationary dryline and intersecting gust fronts: A case study. *J. Geophys. Res. Atmos.*, **124**, 2379–2396, https://doi.org/10.1029/2018JD029832.

Bosart, L. F., W. E. Bracken, and A. Seimon, 1998: A study of cyclone mesoscale structure with emphasis on a large-amplitude inertia–gravity wave. *Mon. Wea. Rev.*, **126**, 1497–1527, https://doi.org/10.1175/1520-0493(1998)126<1497:ASOCMS>2.0.CO;2.

Bretherton, C. S., and P. K. Smolarkiewicz, 1989: Gravity waves, compensating subsidence and detrainment around cumulus clouds. *J. Atmos. Sci.*, **46**, 740–759, https://doi.org/10.1175/1520-0469(1989)046<0740:GWCSAD>2.0.CO;2.

Browning, K. A., and Coauthors, 2007: The convective storm initiation project. *Bull. Amer. Meteor. Soc.*, **88**, 1939–1956, https://doi.org/10.1175/BAMS-88-12-1939.

Bryan, G. H., and R. Rotunno, 2009: The maximum intensity of tropical cyclones in axisymmetric numerical model simulations. *Mon. Wea. Rev.*, **137**, 1770–1789, https://doi.org/10.1175/2008MWR2709.1.

Collins, W., and Coauthors, 2004: Description of the NCAR Community Atmosphere Model (CAM 3.0). NCAR Tech. Note NCAR TN-464+STR, 226 pp., https://doi.org/10.5065/D63N21CH.

Crawford, T. M., and H. B. Bluestein, 1997: Characteristics of dryline passage during COPS-91. *Mon. Wea. Rev.*, **125**, 463–477, https://doi.org/10.1175/1520-0493(1997)125<0463:CODPDC>2.0.CO;2.

Crook, N. A., 1988: Trapping of low-level internal gravity waves. *J. Atmos. Sci.*, **45**, 1533–1541, https://doi.org/10.1175/1520-0469(1988)045<1533:TOLLIG>2.0.CO;2.

Droegemeier, K. K., and R. B. Wilhelmson, 1985: Three-dimensional numerical modeling of convection produced by interacting thunderstorm outflows. Part I: Control simulation and low-level moisture variations. *J. Atmos. Sci.*, **42**, 2381–2403, https://doi.org/10.1175/1520-0469(1985)042<2381:TDNMOC>2.0.CO;2.

Du, Y., and F. Zhang, 2019: Banded convective activity associated with mesoscale gravity waves over Southern China. *J. Geophys. Res. Atmos.*, **124**, 1912–1930, https://doi.org/10.1029/2018JD029523.

Edwards, R., R. L. Thompson, and J. G. LaDue, 2000: Initiation of storm A (3 May 1999) along a possible horizontal convective roll. Preprints, *20th Conf. on Severe Local Storms*, Orlando, FL, Amer. Meteor. Soc., 60–63, https://www.spc.noaa.gov/publications/edwards/hcr3may.htm.

Fan, Z., K. Zhu, and M. Xue, 2023: Decay processes and statistical characteristics of continental northeast China cold vortex from April to September. *Acta Meteor. Sin.*, **81**, 727–740, http://doi.org/10.11676/qxxb2023.20220171.

Fang, Z. L., X. D. Yu, and X. M. Wang, 2020: Statistical analysis of drylines in Northeast China. *Acta Meteor. Sin.*, **78**, 260–276, http://doi.org/10.11676/qxxb2020.024.

Fovell, R. G., 2002: Upstream influence of numerically simulated squall-line storms. *Quart. J. Roy. Meteor. Soc.*, **128**, 893–912, https://doi.org/10.1256/0035900021643737.

——, D. Durran, and J. R. Holton, 1992: Numerical simulations of convectively generated stratospheric gravity waves. *J. Atmos. Sci.*, **49**, 1427–1442, https://doi.org/10.1175/1520-0469(1992)049,1427:NSOCGS.2.0.CO;2.

——, G. L. Mullendore, and S.-H. Kim, 2006: Discrete propagation in numerically simulated nocturnal squall lines. *Mon. Wea. Rev.*, **134**, 3735–3752, https://doi.org/10.1175/MWR3268.1.

Fujita, T. T., 1989: The Teton-Yellowstone tornado of 21 July 1987. *Mon. Wea. Rev.*, **117**, 1913–1940, https://doi.org/10.1175/1520-0493(1989)117<1913:TTYTOJ>2.0.CO;2.

Geerts, B., and Coauthors, 2017: The 2015 plains elevated convection at night field project. *Bull. Amer. Meteor. Soc.*, **98**, 767–786, https://doi.org/10.1175/BAMS-D-15-00257.1.

Haghi, K. R., and Coauthors, 2019: Bore-ing into nocturnal convection. *Bull. Amer. Meteor. Soc.*, **100**, 1103–1121, https://doi.org/10.1175/BAMS-D-17-0250.1.

Koch, S. E., R. E. Golus, and P. B. Dorian, 1988: A mesoscale gravity wave event observed during CCOPE. Part II: Interactions between mesoscale convective systems and the antecedent waves. *Mon. Wea. Rev.*, **116**, 2545–2569, https://doi.org/10.1175/1520-0493(1988)116<2545:AMGWEO>2.0.CO;2.

Lac, C., J.-P. Lafore, and J.-L. Redelsperger, 2002: Role of gravity waves in triggering deep convection during TOGA COARE. *J. Atmos. Sci.*, **59**, 1293–1316, https://doi.org/10.1175/1520-0469(2002)059<1293:ROGWIT>2.0.CO;2.

Lane, T. P., and M. J. Reeder, 2001: Convectively generated gravity waves and their effect on the cloud environment. *J.*

Atmos. Sci., **58**, 2427–2440, https://doi.org/10.1175/1520-0469(2001)058<2427:CGGWAT>2.0.CO;2.

——, and F. Zhang, 2011: Coupling between gravity waves and tropical convection at mesoscales. *J. Atmos. Sci.*, **68**, 2582–2598, https://doi.org/10.1175/2011JAS3577.1.

Lean, H. W., N. M. Roberts, P. A. Clark, and C. Morcrette, 2009: The surprising role of orography in the initiation of an isolated thunderstorm in southern England. *Mon. Wea. Rev.*, **137**, 3026–3046, https://doi.org/10.1175/2009MWR2743.1.

Liu, L., L. Ran, and S. Gao, 2018: Analysis of the characteristics of inertia-gravity waves during an orographic precipitation event. *Adv. Atmos. Sci.*, **35**, 604–620, https://doi.org/10.1007/s00376-017-7159-2.

Luo, L., M. Xue, and K. Zhu, 2020: The initiation and organization of a severe hail-producing mesoscale convective system in East China: A numerical study. *J. Geophys. Res. Atmos.*, **125**, e2020JD032606, https://doi.org/10.1029/2020JD032606.

Mapes, B. E., 1993: Gregarious tropical convection. *J. Atmos. Sci.*, **50**, 2026–2037, https://doi.org/10.1175/1520-0469(1993)050<2026:GTC>2.0.CO;2.

Markowski, P., C. Hannon, and E. Rasmussen, 2006: Observations of convection initiation "failure" from the 12 June 2002 IHOP deployment. *Mon. Wea. Rev.*, **134**, 375–405, https://doi.org/10.1175/MWR3059.1.

Marsham, J. H., S. B. Trier, T. M. Weckwerth, and J. W. Wilson, 2011: Observations of elevated convection initiation leading to a surface-based squall line during 13 June IHOP_2002. *Mon. Wea. Rev.*, **139**, 247–271, https://doi.org/10.1175/2010MWR3422.1.

McAnelly, R. L., J. E. Nachamkin, W. R. Cotton, and M. E. Nicholls, 1997: Upscale evolution of MCSs: Doppler radar analysis and analytical investigation. *Mon. Wea. Rev.*, **125**, 1083–1110, https://doi.org/10.1175/1520-0493(1997)125<1083:UEOMDR>2.0.CO;2.

Meng, Z., and Coauthors, 2016: Wind estimation around the shipwreck of oriental star based on field damage surveys and radar observations. *Sci. Bull.*, **61**, 330–337, https://doi.org/10.1007/s11434-016-1005-2.

Morrison, H., and W. W. Grabowski, 2008: A novel approach for representing ice microphysics in models: Description and tests using a kinematic framework. *J. Atmos. Sci.*, **65**, 1528–1548, https://doi.org/10.1175/2007JAS2491.1.

Nicholls, M. E., R. A. Pielke, and W. R. Cotton, 1991: Thermally forced gravity waves in an atmosphere at rest. *J. Atmos. Sci.*, **48**, 1869–1884, https://doi.org/10.1175/1520-0469(1991)048<1869:TFGWIA>2.0.CO;2.

Parsons, D. B., K. R. Haghi, K. T. Halbert, B. Elmer, and J. Wang, 2019: The potential role of atmospheric bores and gravity waves in the initiation and maintenance of nocturnal convection over the Southern Great Plains. *J. Atmos. Sci.*, **76**, 43–68, https://doi.org/10.1175/JAS-D-17-0172.1.

Pleim, J. E., 2006: A simple, efficient solution of flux–profile relationships in the atmospheric surface layer. *J. Appl. Meteor. Climatol.*, **45**, 341–347, https://doi.org/10.1175/JAM2339.1.

——, 2007: A combined local and nonlocal closure model for the atmospheric boundary layer. Part I: Model description and testing. *J. Appl. Meteor. Climatol.*, **46**, 1383–1395, https://doi.org/10.1175/JAM2539.1.

Powers, J. G., and R. J. Reed, 1993: Numerical simulation of the large-amplitude mesoscale gravity-wave event of 15 December 1987 in the central United States. *Mon. Wea. Rev.*, **121**, 2285–2308, https://doi.org/10.1175/1520-0493(1993)121<2285:NSOTLA>2.0.CO;2.

Rasmussen, K. L., and R. A. Houze Jr., 2016: Convective initiation near the Andes in subtropical South America. *Mon. Wea. Rev.*, **144**, 2351–2374, https://doi.org/10.1175/MWR-D-15-0058.1.

Raymond, D. J., 1987: A forced gravity wave model of serf-organizing convection. *J. Atmos. Sci.*, **44**, 3528–3543, https://doi.org/10.1175/1520-0469(1987)044<3528:AFGWMO>2.0.CO;2.

Schmidt, J. M., and W. R. Cotton, 1990: Interactions between upper and lower tropospheric gravity waves on squall line structure and maintenance. *J. Atmos. Sci.*, **47**, 1205–1222, https://doi.org/10.1175/1520-0469(1990)047<1205:IBUALT>2.0.CO;2.

Scorer, R. S., 1949: Theory of waves in the lee of mountains. *Quart. J. Roy. Meteor. Soc.*, **75**, 41–56, https://doi.org/10.1002/qj.49707532308.

Skamarock, C., and Coauthors, 2019: A description of the Advanced Research WRF Model version 4. NCAR Tech. Note NCAR TN-556+STR, 162 pp., https://doi.org/10.5065/1dfh-6p97.

Stobie, J. G., F. Einaudi, and L. W. Uccellini, 1983: A case study of gravity waves–convective storms interaction: 9 May 1979. *J. Atmos. Sci.*, **40**, 2804–2830, https://doi.org/10.1175/1520-0469(1983)040<2804:ACSOGW>2.0.CO;2.

Su, T., and G. Zhai, 2017: The role of convectively generated gravity waves on convective initiation: A case study. *Mon. Wea. Rev.*, **145**, 335–359, https://doi.org/10.1175/MWR-D-16-0196.1.

Sun, L., X. Y. Zheng, and Q. Wang, 1994: The climatological characteristics of northeast cold vortex in China. *Quart. J. Appl. Meteor.*, **5**, 297–303.

Sun, Z., M. Xue, K. Zhu, and B. Zhou, 2019: Prediction of an EF4 supercell tornado in Funing, China: Resolution dependency of simulated tornadoes and their structures. *Atmos. Res.*, **229**, 175–189, https://doi.org/10.1016/j.atmosres.2019.06.019.

Taylor, N. M., and Coauthors, 2011: The Understanding Severe Thunderstorms and Alberta Boundary Layers Experiment (UNSTABLE) 2008. *Bull. Amer. Meteor. Soc.*, **92**, 739–763, https://doi.org/10.1175/2011BAMS2994.1.

Uccellini, L. W., and S. E. Koch, 1987: The synoptic setting and possible energy sources for mesoscale wave disturbances. *Mon. Wea. Rev.*, **115**, 721–729, https://doi.org/10.1175/1520-0493(1987)115<0721:TSSAPE>2.0.CO;2.

Wang, Q., M. Xue, and Z. Tan, 2016: Convective initiation by topographically induced convergence forcing over the Dabie Mountains on 24 June 2010. *Adv. Atmos. Sci.*, **33**, 1120–1136, https://doi.org/10.1007/s00376-016-6024-z.

Wang, Q.-W., and M. Xue, 2012: Convective initiation on 19 June 2002 during IHOP: High-resolution simulations and analysis of the mesoscale structures and convection initiation. *J. Geophys. Res.*, **117**, D12107, https://doi.org/10.1029/2012JD017552.

——, and ——, 2018: A high-resolution modeling study of the 19 June 2002 convective initiation case during IHOP_2002: Localized forcing by horizontal convective rolls. *Adv. Atmos. Sci.*, **35**, 1243–1253, https://doi.org/10.1007/s00376-018-7218-3.

Weckwerth, T. M., and D. B. Parsons, 2006: A review of convection initiation and motivation for IHOP_2002. *Mon. Wea. Rev.*, **134**, 5–22, https://doi.org/10.1175/MWR3067.1.

——, and Coauthors, 2004: An overview of the International H_2O Project (IHOP_2002) and some preliminary highlights. *Bull. Amer. Meteor. Soc.*, **85**, 253–278, https://doi.org/10.1175/BAMS-85-2-253.

Wei, P., and Coauthors, 2022: On the key dynamical processes supporting the 21.7 Zhengzhou record-breaking hourly rainfall in China. *Adv. Atmos. Sci.*, **40**, 337–349, https://doi.org/10.1007/s00376-022-2061-y.

Weiss, C. C., and H. B. Bluestein, 2002: Airborne pseudo–dual Doppler analysis of a dryline–outflow boundary intersection. *Mon. Wea. Rev.*, **130**, 1207–1226, https://doi.org/10.1175/1520-0493(2002)130<1207:APDDAO>2.0.CO;2.

Wilson, J. W., and D. L. Megenhardt, 1997: Thunderstorm initiation, organization, and lifetime associated with Florida boundary layer convergence lines. *Mon. Wea. Rev.*, **125**, 1507–1525, https://doi.org/10.1175/1520-0493(1997)125<1507:TIOALA>2.0.CO;2.

——, and R. D. Roberts, 2006: Summary of convective storm initiation and evolution during IHOP: Observational and modeling perspective. *Mon. Wea. Rev.*, **134**, 23–47, https://doi.org/10.1175/MWR3069.1.

——, J. A. Moore, G. B. Foote, B. Martner, A. R. Rodi, T. Uttal, and J. M. Wilczak, 1988: Convection Initiation and Downburst Experiment (CINDE). *Bull. Amer. Meteor. Soc.*, **69**, 1328–1347, https://doi.org/10.1175/1520-0477(1988)069<1328:CIADE>2.0.CO;2.

——, S. B. Trier, D. W. Reif, R. D. Roberts, and T. M. Weckwerth, 2018: Nocturnal elevated convection initiation of the PECAN 4 July hailstorm. *Mon. Wea. Rev.*, **146**, 243–262, https://doi.org/10.1175/MWR-D-17-0176.1.

Xie, Z., and C. Bueh, 2015: Different types of cold vortex circulations over northeast China and their weather impacts. *Mon. Wea. Rev.*, **143**, 845–863, https://doi.org/10.1175/MWR-D-14-00192.1.

Xue, M., and W. J. Martin, 2006a: A high-resolution modeling study of the 24 May 2002 dryline case during IHOP. Part I: Numerical simulation and general evolution of the dryline and convection. *Mon. Wea. Rev.*, **134**, 149–171, https://doi.org/10.1175/MWR3071.1.

——, and ——, 2006b: A high-resolution modeling study of the 24 May 2002 dryline case during IHOP. Part II: Horizontal convective rolls and convective initiation. *Mon. Wea. Rev.*, **134**, 172–191, https://doi.org/10.1175/MWR3072.1.

Yuan, C., S. G. Wang, X. Y. Ma, L. Yang, and L. Chen, 2021: Environmental background and formative mechanisms of a tornado occurred in Kaiyuan on 3 July 2019. *Plateau Meteor.*, **40**, 384–393.

Zhang, F., C. A. Davis, M. L. Kaplan, and S. E. Koch, 2001: Wavelet analysis and the governing dynamics of a large-amplitude mesoscale gravity-wave event along the East Coast of the United States. *Quart. J. Roy. Meteor. Soc.*, **127**, 2209–2245, https://doi.org/10.1002/qj.49712757702.

——, Q. Zhang, and J. Sun, 2021: Initiation of an elevated mesoscale convective system with the influence of complex terrain during Meiyu season. *J. Geophys. Res. Atmos.*, **126**, e2020JD033416, https://doi.org/10.1029/2020JD033416.

Zhang, T., and Coauthors, 2020: Damage survey of the 3 July 2019 Kaiyuan Tornado in Liaoning province and its evolution revealed by disaster. *Meteor. Mon.*, **46**, 603–617, http://doi.org/10.7519/j.issn.1000-0526.2020.05.002.

Zheng, Y., and Coauthors, 2020: Environmental conditions, evolution and mechanisms of the EF4 Tornado in Kaiyuan of Liaoning province on 3 July 2019. *Meteor. Mon.*, **46**, 589–602, http://doi.org/10.7519/j.issn.1000-0526.2020.05.001.

Zhu, K., and M. Xue, 2016: Evaluation of WRF-based convection-permitting multi-physics ensemble forecasts over China for an extreme rainfall event on 21 July 2012 in Beijing. *Adv. Atmos. Sci.*, **33**, 1240–1258, https://doi.org/10.1007/s00376-016-6202-z.

——, and Coauthors, 2018: Evaluation of real-time convection-permitting precipitation forecasts in China during the 2013–2014 summer season. *J. Geophys. Res. Atmos.*, **123**, 1037–1064, https://doi.org/10.1002/2017JD027445.